Journal of *Marine Science and Engineering*

MDPI

Article

Assessment of Shoreline Change from SAR Satellite Imagery in Three Tidally Controlled Coastal Environments

Salvatore Savastano [1,*], Paula Gomes da Silva [2], Jara Martínez Sánchez [2], Arnau Garcia Tort [2], Andres Payo [3], Mark E. Pattle [1], Albert Garcia-Mondéjar [1], Yeray Castillo [4,5] and Xavier Monteys [6]

1 isardSAT UK, Guildford GU2 7YG, UK; mark.pattle@isardsat.co.uk (M.E.P.); albert.garcia@isardsat.co.uk (A.G.-M.)
2 IHCantabria—Instituto de Hidráulica Ambiental, Universidad de Cantabria, 39011 Santander, Spain; gomesp@unican.es (P.G.d.S.); jara.martinez@unican.es (J.M.S.); arnau.garcia@unican.es (A.G.T.)
3 British Geological Survey, Nottingham NG12 5GG, UK; agarcia@bgs.ac.uk
4 Department of Geography, National University of Ireland Maynooth, W23 X021 Maynooth, Ireland; yeray.castillocampo.2023@mumail.ie
5 Department of the Environment, Climate and Communications, Geological Survey Ireland, A94 N2R6 Dublin, Ireland
6 Marine and Coastal Unit, Geological Survey Ireland, A94 N2R6 Blackrock, Ireland
* Correspondence: salvatore.savastano@isardsat.co.uk

Abstract: Coasts are continually changing and remote sensing from satellites has the potential to both map and monitor coastal change at multiple scales. Unlike optical technology, synthetic aperture radar (SAR) is uninfluenced by darkness, clouds, and rain, potentially offering a higher revision period to map shoreline position and change, but this can only be feasible if we have a better interpretation of what shorelines as extracted from SAR imagery represent on the ground. This study aims to assess the application of shorelines extracted from SAR from publicly available satellite imagery to map and capture intra-annual to inter-annual shoreline variability. This is assessed in three tidally controlled coastal study areas that represent sand and gravel beaches with different backshore environments: low-lying dunes and marsh; steep, rocky cliff; and urban environments. We have found that SAR shorelines consistently corresponded to positions above the high-water mark across all three sites. We further discuss the influence of the scene geometry, meteorological and oceanographic conditions, and backshore environment and provide a conceptual interpretation of SAR-derived shorelines. In a low-lying coastal setting, the annual change rate derived through SAR presents a high degree of alignment with the known reference values. The present study contributes to our understanding of the poorly known aspect of using shorelines derived from publicly available SAR satellite missions. It outlines a quantitative approach to automatically assess their quality with a new automatic detection method that is transferable to shoreline evolution assessments worldwide.

Keywords: coastal erosion; Earth observation; remote sensing; shoreline; SAR

Citation: Savastano, S.; Gomes da Silva, P.; Sánchez, J.M.; Tort, A.G.; Payo, A.; Pattle, M.E.; Garcia-Mondéjar, A.; Castillo, Y.; Monteys, X. Assessment of Shoreline Change from SAR Satellite Imagery in Three Tidally Controlled Coastal Environments. *J. Mar. Sci. Eng.* **2024**, *12*, 163. https://doi.org/10.3390/jmse12010163

Academic Editor: Gerben Ruessink

Received: 6 December 2023
Revised: 9 January 2024
Accepted: 11 January 2024
Published: 15 January 2024

1. Introduction

Coastal areas are subject to several natural and human-induced changes. The increasing apprehension worldwide revolves around the anticipated alterations and potential threats to individuals, ecosystems, and the natural environment [1]. Understanding the dynamic nature of coastal areas and predicting future behaviors is crucial for informed planning decisions. Quantifying physical changes along shorelines and their response to human actions plays a pivotal role in this endeavor. Often, the rates of physical change are expressed in various units [2], with the common measure being meters per year. While shoreline is loosely defined as the meeting point of water and land surfaces, its dynamic nature and dependence on temporal and spatial scales necessitate the use of different shoreline indicators. These indicators can be observed with diverse techniques and technologies [3,4].

Over the past 38 years, remote sensing and satellite technology have been used to monitor coastal areas, offering an abundant resource for obtaining historical shoreline datasets spanning various spatial scales. These datasets can range from small-scale localized studies to groundbreaking global applications, exemplified by the endeavors of [5,6]. In this domain, two types of satellite imagery play a crucial role: multi-spectral images (optical) and synthetic aperture radar (SAR) images.

The former, often referred to as a "passive sensor", captures data within the optical bandwidth. When a scene is illuminated by sunlight or another light source, different materials absorb and reflect light in distinct ways, creating specific spectral signatures. These unique patterns of reflected light at various wavelengths can be combined to generate indicators capable of discerning the boundary between land and sea [7–10]. Nonetheless, optical sensors come with several limitations. The precision and frequency of coastal change measurements are compromised when cloud cover or other atmospheric conditions obstruct the area of interest. Countries like the United Kingdom, Ireland, or northern Spain (Cantabrian Sea) experience persistent cloud cover throughout much of the year. Consequently, despite numerous optical satellite acquisition operations, only a few provide valuable data for establishing reliable shorelines.

As opposed to optical sensors, SAR is an "active" microwave imaging system, belonging to a wider family of imaging radars, generically named side-looking airborne radars. It is mounted on a platform moving at a constant velocity along a trajectory (azimuth direction) [11]. During its movement, the sensor transmits a sequence of closely spaced electromagnetic waves at regular intervals towards the Earth. These high-power pulses traveling at the speed of light along the line of sight radar–target (slant range) interact with the Earth's surface, and in most cases, their energy is partially re-irradiated back (backscattered) to the receiving antenna a short time later at a slightly different location, as the satellite travels along its orbit. During the step of recording the signal backscattered from the surface, both its amplitude and phase are considered, and they depend on the physical (i.e., geometry, roughness) and electrical properties (i.e., permittivity) of the imaged scene [12] but also on radar system parameters, such as electromagnetic wave polarization (horizontal or vertical) of transmitting and receiving antennas or transmitted power. A complex focusing technique applied to all the recorded signals generates a 2D reflectivity map that can be used to discriminate among targets depending on the strength of the backscattered signal [13].

Although many image processing techniques have been developed for shoreline extraction using SAR imagery, it is not entirely understood to what extent the signal returned from the sea surface differs from that received from the adjacent land surface. This fundamental disparity stands as one of the most critical factors affecting the detection of the land–sea boundary. Most shoreline detection techniques rely on this difference in the returned signal from the land and the sea. The contrast between the land and the sea is significantly influenced by many factors, including the polarization method used for transmitting and receiving the electromagnetic waves, the land morphology (presence/absence of cliffs or dune systems), and the sea surface conditions. The polarization method used for transmitting and receiving electromagnetic waves determines the strength of the backscatter from the land or sea, which affects the contrast between the two. The land morphology can cause shadows or reflections, which further affect contrast. The sea surface conditions, such as waves and foam, also have a significant impact on contrast. Also, SAR images are affected by speckle, a multiplicative noise that gives the images a grainy appearance and makes interpretation more challenging than with optical images.

Furthermore, most of the above-mentioned techniques have been employed using a restricted number of SAR scenes. To the best of the authors' knowledge, no comprehensive utilization of the abundant public satellite imagery has been implemented to investigate and assess shoreline evolution over time through SAR as it has been performed with optical imagery [14]. In previous works [15,16], an initial effort was made to interpret SAR shorelines (hereinafter SLs) by comparing them with SLs extracted from optical satellite

data. The studies utilized publicly available satellite imagery to explore how effectively these two technologies can map and capture SL variations on a sub-annual to inter-annual basis. Although the studies yielded interesting results, the authors acknowledged the potential for misleading comparisons due to the complexity of SAR images. Consequently, they emphasized the need for further analysis to gain a comprehensive understanding of what SAR observes.

Motivated by the unresolved questions surrounding SAR, this paper seeks to enhance our comprehension of SAR capabilities by thoroughly investigating the ground-based features detected in SLs in thousands of images collected between 2015 and 2021. To achieve this goal, a novel approach is introduced, involving both qualitative and quantitative analyses of SAR-derived SLs. This approach includes an improved processing chain for SL extraction and a series of validation methods to ensure the accuracy and reliability of the results. The manuscript offers a comprehensive overview of the SAR product utilized in this analysis and presents a detailed explanation of the steps involved in extracting shorelines from SAR data. The various filters applied to the SAR product, as well as the "qualitative" outcomes that can be achieved with this technology, are discussed. Subsequently, the study introduces three distinct sites with different environments, namely, a flat beach (Bull Island); high dunes of sand (Salinas beach); and a steep, rocky cliff (Start Bay). Each site undergoes a validation process tailored to its unique characteristics, enabling a "quantification" of what SAR detects over time. The manuscript concludes with a discussion of the findings, providing valuable insights into the lesser-understood aspects of utilizing SL data derived from publicly available SAR satellite missions.

2. Materials and Methods

Figure 1 summarizes the methodology employed in this study. SAR satellite images from Sentinel-1 (S1) that cover the three study sites are downloaded and preprocessed to ensure their suitability for subsequent processing. Subsequently, SAR-SLs are extracted and used to obtain two quality indicators: heatmaps and distances from the reference line (RL). These indicators are employed to filter SL vectors with the aim of improving the ability to detect coastal changes based on them (see Section 2.4.2). Finally, the resultant SAR-SL time series are subjected to a quantitative assessment based on the comparison with ground-truth data and on the assessment of their ability to represent SL changes. To achieve this, a suitable, tailored validation technique is applied to consider the distinct characteristics of each study site.

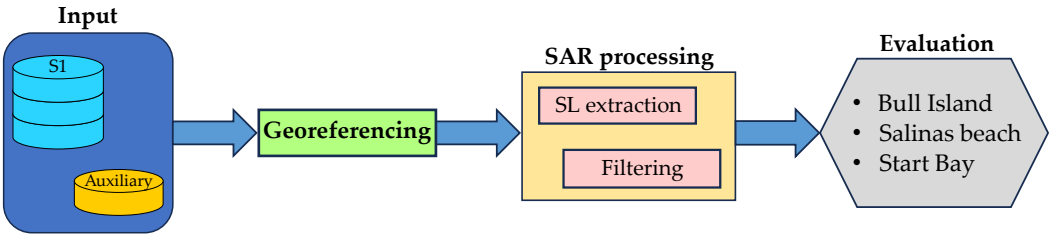

Figure 1. Overall methodology used to assess shoreline change from SAR satellite imagery in three macro-tidal coastal environments. SAR-S1 data, combined with auxiliary data, are used to extract SAR-SLs, distances from the reference line (RL), and annual change rates. Interpretation of SAR-SLs is performed for three different locations.

2.1. Study Zones

We have selected three different tidally controlled coastal areas in Great Britain, Ireland, and Spain which include sand and gravel beaches backed up by three different environments: low-lying dunes and marsh (Bull Island in Ireland); steep, rocky cliff (Start Bay in Great Britain); and high, sandy dunes (Salinas in Spain) (Figure 2). All three study areas also capture different morphodynamic behaviors and cloud coverage conditions. The details of each study site are described in detail here.

In all the selected locations, cloud cover represents the main limitation to utilizing optical data for monitoring coastal evolution. There are only a limited number of optical images available for each site, making it extremely challenging to build a sufficiently extensive time series. Although SAR images cannot directly be compared to optical images due to speckle noise and geometry artifacts, they provide reliable temporal sampling (20 images per month for the S1 constellation). In Table 1, we compare the data availability between the optical satellite Sentinel-2 (S2) and the SAR S1 missions, both of which have been developed by the European Space Agency (ESA) as part of the Copernicus program.

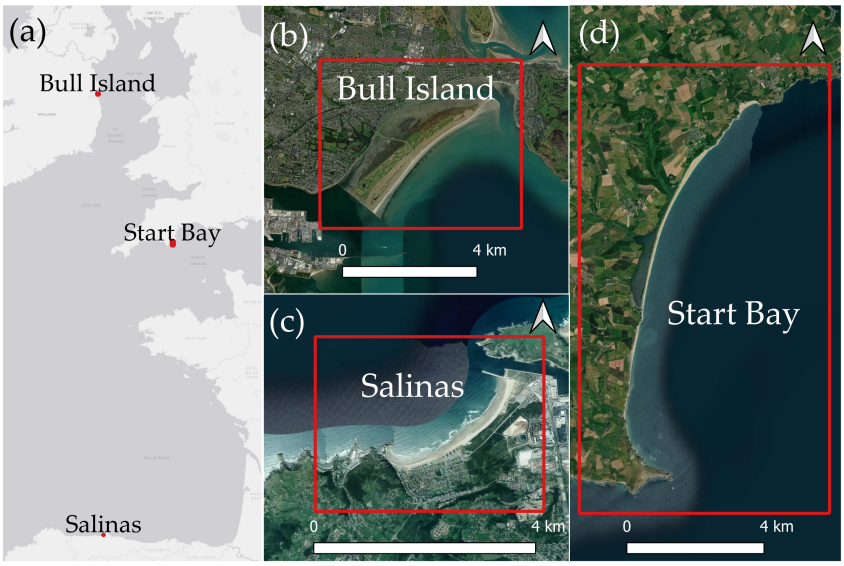

Figure 2. Location of study sites (**a**) on a map of Great Britain, Ireland, and Spain: (**b**) the Bull Island study site in Dublin Bay in Ireland; (**c**) Salinas beach in the north of Spain; and (**d**) the Start Bay study site in the south of England, Great Britain. Source of aerial imagery: Esri, Maxar, GeoEye, Earthstar Geographics, CNES/Airbus DS, USDA, USGS, AeroGRID, IGN, and the GIS User Community (v10.6). BGS ©UKRI.

Table 1. A comparison of the SAR data available for each site under analysis with the S2 data with 0% cloud coverage.

	Bull Island	**Salinas Beach**	**Start Bay**
Optical (S2)	76	125	53
SAR (S1)	1055	1411	1402

2.1.1. Bull Island: Flat, Sandy Beach Backed by Low-Lying Dunes and Marsh

Bull Island is a low-lying island in the northern part of Dublin Bay, Dublin, eastern Ireland. It is a 5 km long, wedge-shaped barrier beach/sand spit extending northeastwards from Dublin Port which developed following the construction of the north port wall during the first half of the 19th century. The island shelters two inter-tidal lagoons divided by a causeway. The system ranges, in width, between 1 km at its southwestern end and 200 m at the northeastern end. It encompasses a continuous, modern foredune system ranging, in height, from 2 to 4 m along the proximal end to more than 9 m in the central–northeastern region towards the distal end. Salt marshes extend along the length of the landward shores. These mud and sandflats inter-tidal areas are regularly inundated by seawater and are fully covered by spring tides. The tidal range in the bay is approximately 3.4 m for spring tides and 1.9 m for neap tides. The prevalent tidal pattern is clockwise circulation with a strong eastwards net flow. The prevalent wave direction in the bay is from SSE with average significant wave heights of 0.35 m [17].

2.1.2. Salinas: Sandy Beach Backed by High Dunes

Salinas beach is located on the Cantabrian Sea, on the left bank of the estuarine inlet of Avilés, in the municipality of San Juan de Navas (Spain). It is 2.5 km long and lies between the inlet jetty to the east and a rocky headland to the west. The eastern half of the beach is backed by sand dunes up to 15 m in height above the mean sea level, whereas the western half is located in the urban area of Salinas, where the beach is backed by a seawall (Figure 2c). The changes in beach morphology in the western part are strongly limited by the sea wall, and because of that, our analysis is mainly focused on the changes observed in those profiles with dunes at the back of the beach. Beach sediment is composed of fine to medium sand. This zone is under semidiurnal tides with approximately 5 m of spring tidal range, and it is exposed to the prevailing northwestern winter swells. Salinas beach usually shows intermediate morphodynamic states that vary from rhythmic bar and beach to skewed transverse bar and rip [18], with a large dissipative domain.

2.1.3. Start Bay: Gravel Beach Backed by Lagoon and Steep, Rocky Cliffs

Start Bay is a 12 km long embayment aligned SSW-NNE and located on the southern coast of Devon, South West England (UK), where the effects of erosion, accretion, and beach rotation have been well studied and documented [19,20]. Meso- to macro-tidal with neap and spring tidal ranges of 1.8 m and 4.3 m, respectively, the embayment comprises five sub-embayment gravel barrier beaches, named, from south to north, Hallsands, Beesands, Slapton Sands, Forest Cove, and Blackpool Sands. Between each pair of sub-embayments lie short headlands/rocky outcrops. Within Start Bay, gravel is finer to the east due to the lateral grading of material [21], with coarser grains being transported southwest with larger, easterly waves and finer grains being well sorted and transported northeast with smaller but more frequent southerly swells. The tidal range can reach up to 6 m, and the wave climate in Start Bay is modulated by Start Point, a rocky headland offering shelter from longer-period southerly waves, and Skerries Bank, an offshore banner bank that sits east of the main beaches in the southern half of the embayment and is −5 m Ordnance Datum Newlyn at its shallowest. Furthermore, the entirety of Start Bay is bound by large headlands, and the system is considered a closed sediment cell, with no sediment sources except for some confined areas of cliff erosion [19]. Total sediment budgets (supra- to sub-tidal), with spatially varying uncertainty levels, indicate that two-thirds of total sediment flux occurs in the supra-tidal area; that beach rotation first occurs within sub-embayments; and that additional sustained and extreme energy levels are then required for full embayment rotation to occur, with significant headland bypassing [19]. The occurrence of these beach rotation events is attributed [22] to a higher frequency of southerly storms and/or a lower frequency of easterly storms over a given time period. Thus, the development and stability of the beach on annual timescales depend on the relative contributions of the two storm types and their sequencing.

2.2. SAR Imagery Datasets

Our study makes use of S1 Level-1 Ground Range Detected (GRD) products, which are freely available at https://search.asf.alaska.edu/#/ (accessed on 6 December 2023) in high resolution or medium resolution (see Table 2). These data consist of SAR data that have been detected, multi-looked, and projected using the WGS84 Earth ellipsoid model. S1 consists of two satellites, which operate at C-band frequency (5.4 GHz), supporting both single (HH or VV) and dual polarization (HH + HV or VV + VH). SAR satellites typically follow two types of orbits: ascending (ASC), in which the satellite travels from the South Pole to the North Pole, and descending (DESC), in which it travels in the opposite direction. Each time the satellite orbits the Earth, it covers the same geographic area twice, once during the ASC pass and once during the DESC pass. As a result, an SAR application can acquire more frequent data over a specific area, which is particularly beneficial for monitoring dynamic processes or rapidly changing environmental conditions. The S1-SAR

instrument acquires data in four exclusive modes [23] that differ in resolution, coverage, and revisit time:

- Stripmap (SM). This is a standard SAR stripmap imaging mode where the ground swath is illuminated with a continuous sequence of pulses and with the antenna beam pointing to fixed azimuth and elevation angle.
- Interferometric wide swath (IW). Data are acquired in three swaths using the terrain observation with progressive scanning SAR (TOPSAR) imaging technique. In IW mode, bursts are synchronized from pass to pass to ensure the alignment of interferometric pairs.
- Extra wide swath (EW). Data are acquired in five swaths using the TOPSAR imaging technique. EW mode provides very large swath coverage at the expense of spatial resolution.
- Wave (WV). Data are acquired in small stripmap scenes called "vignettes", situated at regular intervals of a 100 km long track. The vignettes are acquired by alternating, acquiring one vignette at a near-range incidence angle and the next vignette at a far-range incidence angle (no WV images available for the study sites).

Table 2. High- and medium-spatial-resolution Level-1 GRD.

	HR (m × m)	MR (m × m)
SM	23 × 23	84 × 84
IW	20 × 22	88 × 87
EW	50 × 50	93 × 87

Based on the number of available data and to ensure consistency and eliminate differences arising from varying data resolutions, among the options, for this study, we chose high-resolution products in IW mode with dual polarization (VV + VH). This choice offers the best resolution to the revisit time ratio, with a minimum revisit time of six days and 20 m × 22 m spatial resolution, acceptable for coastal monitoring purposes. Figure 3a illustrates, as an example, the available datasets for the Start Bay study site (comparable numbers are also obtainable for the other two sites). The selected product for Start Bay provides a total of 1734 images for the period for which S1-SAR data are available, from April 2014 to July 2023 (e.g., 192 images per year for 9 years). Moreover, the authors decided to use VH polarization rather than VV polarization due to its lower sensitivity to sea conditions and improved contrast between land and sea, as depicted in Figure 3b,c. This preference was further substantiated by a quantitative analysis presented in [24] to determine the best-suited polarization for these scenarios.

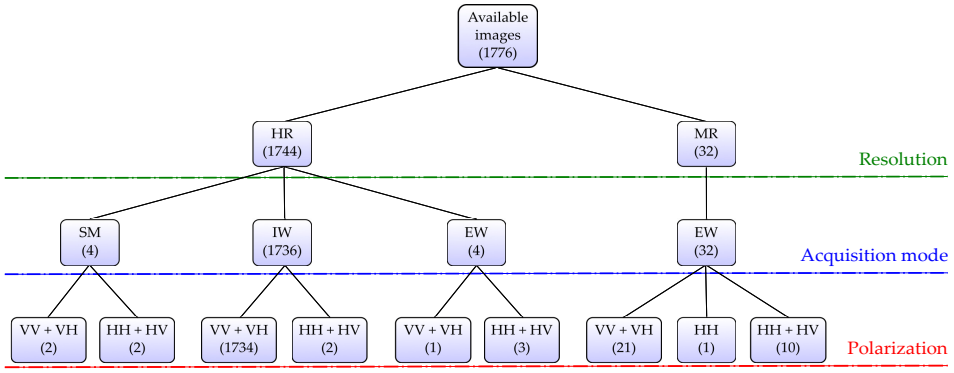

(**a**)

Figure 3. *Cont.*

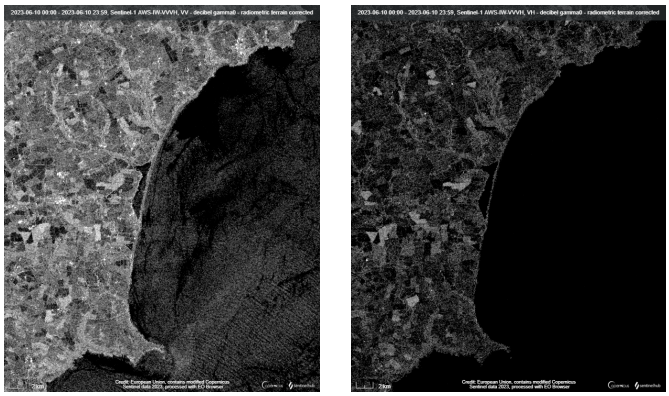

(**b**) (**c**)

Figure 3. Available S1 Level-1 Ground Range Detected datasets for Start Bay as of 31 July 2023. In brackets, the number of available images is reported (**a**); examples of S1 VV (**b**) and VH (**c**) acquisition in Start Bay (UK), 10 June 2023. Credit: European Union, contains modified Copernicus Sentinel data 2023, processed with EO Browser.

2.3. Georeferencing SAR Images

The process of extracting SL and computing rates of SL change from SAR imagery is depicted in the flowchart shown in Figure 4.

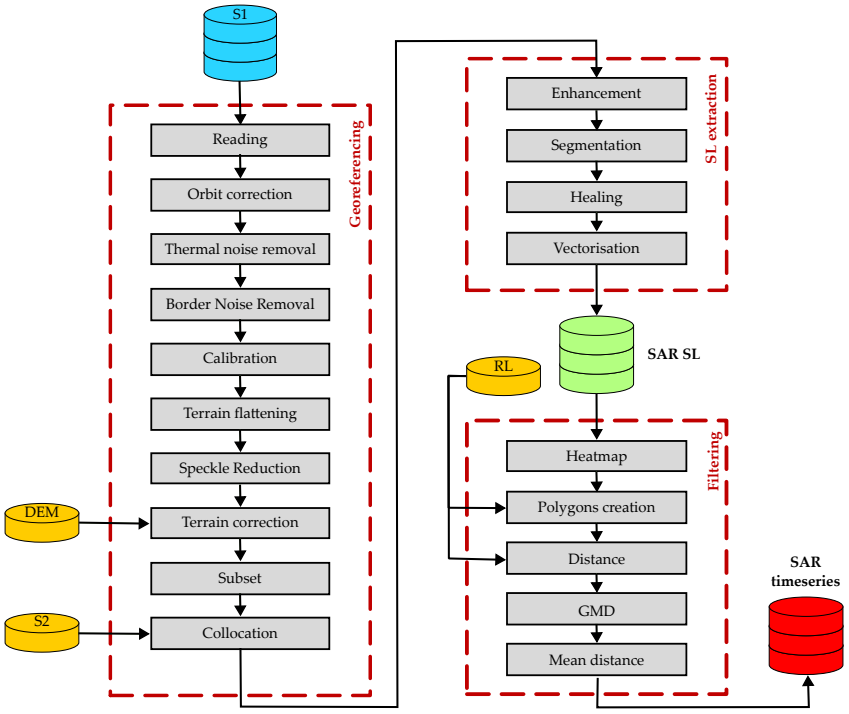

Figure 4. SAR processing flowchart used in this study showing the three main consecutive steps of georeferencing, SL extraction, and filtering.

Initially, S1-SAR data are processed to produce a georeferenced image using the tools provided by the Sentinel Application Platform developed by the ESA [25]. Double correction is applied to the signal to remove noise (thermal and border noise) after updating the orbit state vectors provided in the metadata of SAR data (applying the orbit file). Next, radiometric correction is applied to the data so that the pixels in the SAR images represent the radar backscatter of the reflecting surface (calibration). Another radiometric calibration (terrain flattening) is applied to reduce the distortions caused by different local incidence angles on the scene under observation. Using the digital elevation model from the Shuttle

Radar Topography Mission (SRTM), this tool recalculates the actual radiometry based on the area illuminated per pixel, thereby limiting the effect of topography on backscatter intensity. A despeckling filter is applied to the SAR image to mitigate the speckle effect, which results in a degradation of the resolution and improves the image's interpretability. There are several speckle filters available on the Sentinel Application Platform. In this study, we use the Lee Sigma filter [26]. This particular filter offers a balance between maintaining spatial resolution and preserving edges, making it a favorable choice [24,27,28]. Following a conversion from linear to decibel (dB) scale, as highlighted in [24], terrain correction is applied to the data. This tool corrects the geometric distortions caused by topography, such as foreshortening and shadowing, which are responsible for geolocation errors. Based on the same elevation model used in terrain flattening, terrain correction moves image pixels into proper spatial relationships with each other. The final step is collocation. Using an optical image from S2, previously reprojected in the same coordinate reference system (WGS84) and resampled, all the SAR images are "collocated", overlapping them with the same S2 image.

2.4. SAR-SL Production and Quality Control Indicators

This process consists of two main sequential stages, named (1) SL extraction and (2) SL filtering (see Figure 4). The final product consists of a database of time-stamped and quality-scored SAR-derived SLs and rates of change for the user-defined polygon areas along the coast. In the following, a detailed description of the above-mentioned steps is provided.

2.4.1. Shoreline Extraction

During the first stage, erroneous features that might appear in the SAR image are eliminated, and a shoreline vector is obtained. The task consists of four sub-tasks: enhancement, segmentation, healing, and vectorization. We employ two algorithms in the enhancement process, wavelet decomposition denoising [29] and anisotropic diffusion [30]. In both methods, the speckle in SAR images is further reduced, while the structural features and textural information of the scene are maintained. During segmentation, a binary raster is generated as an initial estimate of the land–sea boundary. Based on the calculation of an appropriate intensity threshold, pixels belonging to the land and the sea can be separated. In this study, the Kittler method [31] is employed to determine this threshold. The binary raster is then improved using binary morphology operations [32]. Binary opening removes foreground features caused by bright reflections from waves or vessels. Next, a minimum size filter is applied, which removes, from the raster, contiguous foreground areas that do not reach a specific number of pixels defined previously by the user. The last step is to fill in the holes within the foreground features. During the last sub-task (vectorization), a shoreline vector is generated from the healed binary raster. This is accomplished by using the marching squares algorithm [33]. A blurring option is implemented prior to applying the latter, which allows the vector to be smoothed to sub-pixel precision and reduces aliasing. Upon completing the extraction stage, a 1D vector line (SL) is produced from each input SAR image, consisting of a sequence of points identified by their geographic coordinates (latitude–longitude).

2.4.2. Shoreline Filtering Based on Distance from the Reference Line

For the second stage of the process, a novel approach has been developed. Its aim is to adequately select some of the points along the previously extracted SAR-SLs to generate a final product that can capitalize patterns of shoreline changes over time. The new method is composed of five steps: (1) heatmapping, (2) polygon creation, (3) point-to-line distance calculation, (4) calculation of Gaussian mixture distribution (GMD), and (5) mean distance.

The first step, heatmapping, enables us to understand how the SLs are distributed in the scene under investigation. As a result of the previous collocation step, all the points along the SLs are aligned in a structured grid-like fashion. By examining both ASC

and DESC tracks, for each point along the SLs, the number of lines passing through it is counted. This value is expressed in percentages based on the total number of lines (ASC plus DESC). The heatmap provides information regarding the dispersion of the SLs and aids in identifying relevant patterns in the scene. For further reduction in speckle, an initial filter based on the heatmap values may be applied for removing points located considerably far from the main concentration of SLs. Figure 5a illustrates an example of a heatmap where each color represents a percentage range. The points affected by noise (visible as white and pink dots) are easily identified, and once the noise has been removed, the primary concentration of SLs becomes evident (Figure 5b).

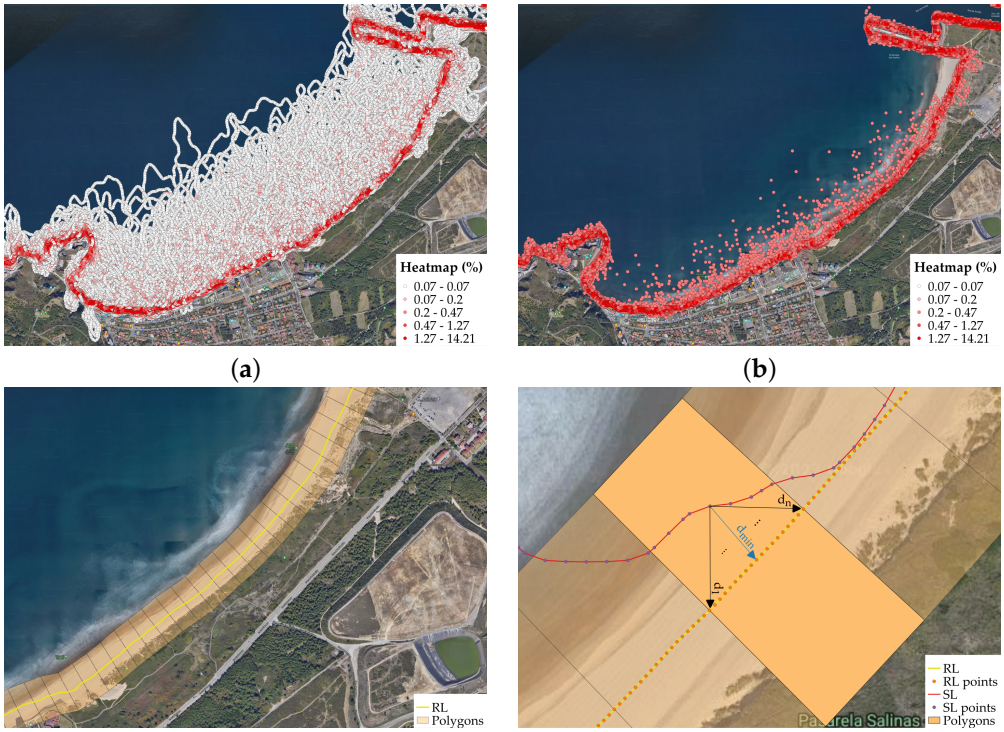

Figure 5. Shoreline filtering for Salinas beach: (**a**) heatmap distribution considering all SL points; (**b**) points following an initial filtering process, revealing a distinct and clear SL pattern; (**c**) polygon creation; (**d**) distance between each SL point and the RL (**b**). Source of aerial imagery: Google, ©2023 Maxar Technologies.

The second step of polygon creation aims to simplify this analysis. The site under investigation is divided into a series of adjacent polygons (Figure 5c). These polygons are constructed along an RL, which can be either provided by the user or derived from the heatmap by observing the SL concentration values. The polygons are oriented perpendicularly to the RL. Their width (w) can be adjusted based on the user's preference, while their length (l) is determined either by the distribution of SLs and associated heatmaps or as per the user's request. It is recommended to include at least the points with higher heatmap values, excluding those that are far from the main concentration, which is often attributed to noise. Except in some complex geometries of the RL (in such cases, overlapping is inevitable), the polygons do not intersect with each other.

In the third step, for each polygon, the distance (d_i) between each point along the SL and the RL, within the boundaries of the respective polygon, is calculated. This distance represents the minimum separation between individual SL points and the RL points. Figure 5d illustrates an example of this calculation. Additionally, a sign is associated with the distance; when a point along the SL is located seaward with respect to the RL, a positive sign is assigned to its distance value, whereas a negative sign is given when it is positioned landward with respect to the RL.

Then, the SL points are filtered using the GMD technique. The SL distances (d_i) are assumed to be described statistically by a Gaussian model with m components. Each component of a mixture is defined by its mean, covariance, and mixing proportions. The Bayes information criterion (BIC) [34] is used to define the appropriate number of components for fitting data. The GMD with the lowest BIC is considered the most suitable model. Once the optimal number of components is determined, the Gaussian distribution with the largest population is considered, and its mean (μ_d) and standard deviation (σ_d) are calculated in a way that only distances (d_i) that satisfy the following expression are considered:

$$\mu_d - 2\sigma_d \leq d_i \leq \mu_d + 2\sigma_d \quad (1)$$

An example of GMD filtering is shown in Figure 6. When the SLs are well concentrated within a polygon, a GMD with a single component is sufficient to statistically describe their distances, as demonstrated in Figure 6a,b. In contrast, for more dispersed distributions, a GMD with multiple components is necessary, as showcased in Figure 6c,d.

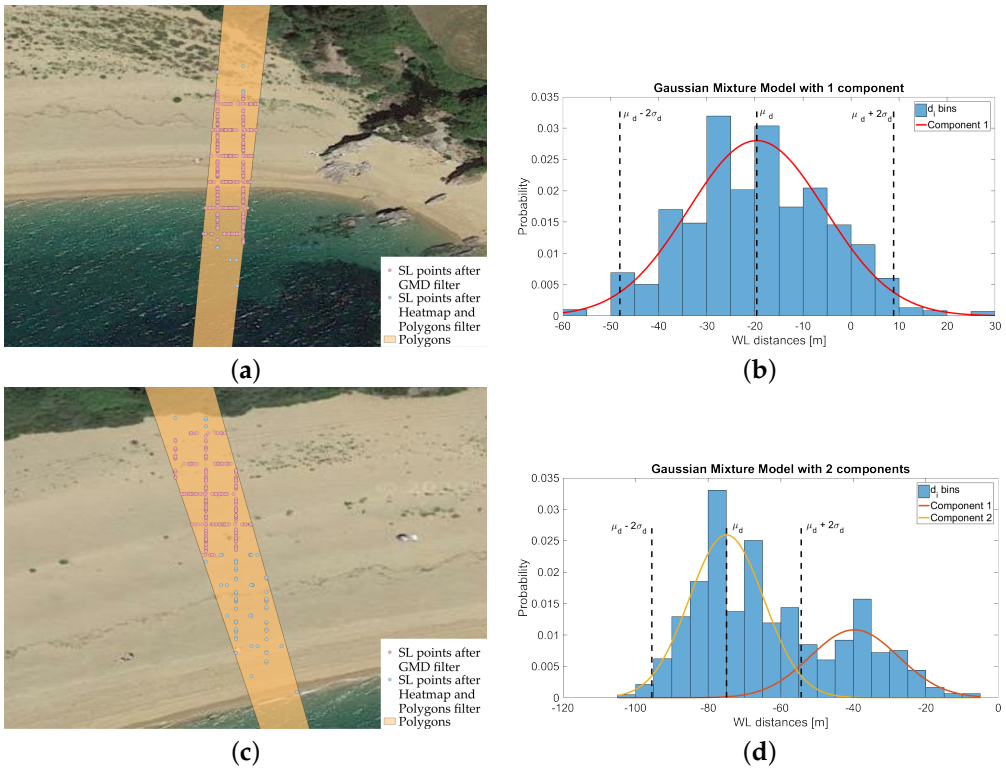

Figure 6. Illustration of Gaussian mixture distribution (GMD) technique for two examples showing a single distribution (**a**,**b**) and a GMD with multiple components (**c**,**d**) for the Start Bay study case. Panels (**a**),(**c**) show the polygons as light-orange-shaded areas and the SL points after filters. The points after the heatmap and polygon filters are indicated as blue circles, and the the ones after the GMD as pink circles. Panels (**b**,**d**) show the histograms of the distances from the reference line distribution for the examples shown in panels a and c, respectively. Source of aerial imagery: Google Satellite Hybrid.

The final stage involves computing the mean distance value (d_M) for each SL by grouping all filtered distance points associated with each SL within individual polygons, thus assigning a distinct value to each SL. This value is assumed to indicate the SL position, and from all SLs, we obtain a time series of d_M which is suitable for detecting shoreline changes over time. Additionally, in each polygon, a linear regression is applied to the filtered SLs' mean d_M. The slope of the regression line represents the change rate for that

polygon, expressed in m/year. The positive or the negative sign of the slope indicates accretion or erosion over time, respectively.

2.5. Validation and Interpretation of SAR Shorelines and Change Rates

SAR-SLs and rates of SL change were interpreted and validated, when possible, for the three study areas considered in this work. The validation process was designed to consider the different environmental characteristics of each study site and included comparing coastal changes estimated from SAR-SLs and those estimated from ground-truth data. In the following, we describe the validation and interpretation assessment undertaken at Bull Island, Salinas beach, and Start Bay.

2.5.1. Bull Island

The foredune system presents a semicontinuous vegetation cover along the seaward front. The coastal extent of terrestrial vegetation is a commonly accepted proxy used to represent the shoreline for coastal change assessments in soft coasts [35]. In this assessment, SL annual change rates (CRs) were calculated using six very-high-resolution satellite images acquired on dates between 01 June 2016 and 01 March 2022 (see Table 3 for details).

Table 3. List of satellite images in the DSAS analysis for Bull Island (Ireland) and their spatial resolution.

Date Acquisition	Source	Provider	Resolution (m × m)
2 June 2016	Google Earth Pro	SPOT 6	6 × 6
7 May 2017	Google Earth Pro	SPOT 7	6 × 6
24 June 2018	Google Earth Pro	WV2 Maxar technologies	2 × 2
1 June 2020	Google Earth Pro	WV2 Maxar technologies	2 × 2
26 April 2021	Google Earth Pro	WV2 Maxar technologies	2 × 2
28 March 2022	Google Earth Pro	WV2 Maxar technologies	2 × 2

The vegetation line (VL) for each available image was manually digitized in Google Earth Pro. The methodological workflow can be summarized in three steps:

1. VL digitizing for each available image.
2. Position and measurement uncertainty calculation.
3. Quantifying SL change employing a dedicated software tool.

A dedicated tool, Digital Shoreline Analysis System (DSAS) [36], designed by the United States Geological Survey (USGS) is used to quantify SL change. A baseline is drawn parallel to the SL, along which perpendicular transects are derived spaced at regular intervals of 50 m. Specific SL change statistics are then calculated along these transects where they intersect with the VL. These rates, expressed in m/year, are calculated using several statistical methods based on measured differences between SL positions. The primary index rate used in this analysis is weighted linear regression (WLR), whereby the more reliable data are given greater emphasis or weight in determining the average yearly SL CRs [37]. The overall shoreline uncertainty accounts for image position and measurement uncertainties, which are factored into the model calculations. Image positional uncertainties in this research range are below 2 m based on the geo-accuracy assessment. Measurement uncertainties, fundamentally derived from digitizing the vegetation line, have been estimated to be 1 m. The resulting shoreline change rate uncertainty, using a 90% confidence interval, has been estimated to be in the range of ±4 m/year [38].

2.5.2. Salinas Beach

At the western boundary of Salinas beach (profiles No. 57 to No. 61 in Figure 7), changes in the dry beach area are limited due to the existing seawall on the backshore. Therefore, all analyses in this study site are associated with changes observed at the eastern boundary of the beach (profiles No. 1 to No. 9 in Figure 7), next to the inlet groin.

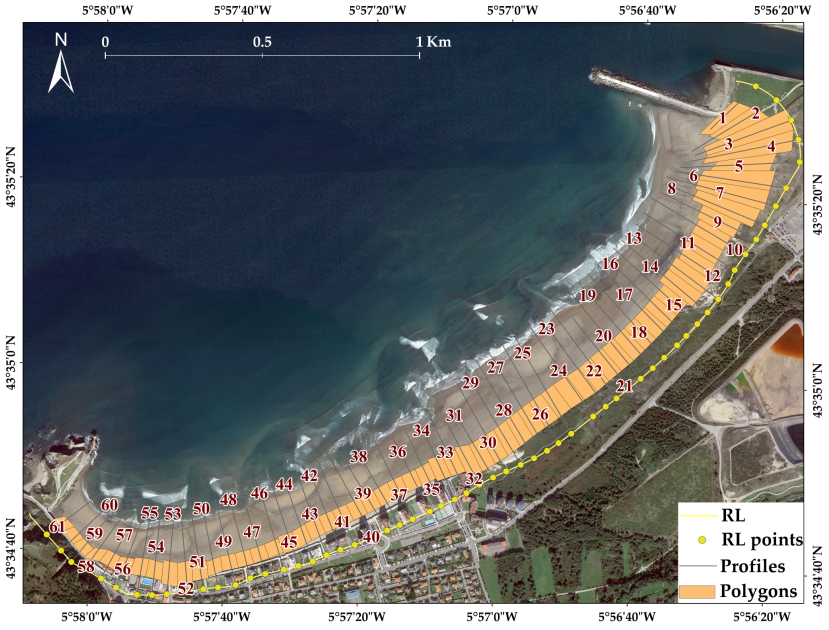

Figure 7. SAR polygons and beach profiles, indicated by numbers, for Salinas beach. Source of aerial imagery: Esri, World Imagery Metadata.

The analyses are made based on the distances of SAR-SLs from the reference line located landward of the dune (green dots in Figure 7) (d_M; see Section 2.4.2). The ability of SAR-SLs to detect morphological changes in the beach profile is assessed at two different timescales:

- Inter-annual changes based on a qualitative assessment of the erosional/accretional processes observed according to the SAR-SL distance from the baseline in comparison to those observed in topographic field surveys. The beach subaerial topography is monitored on a regular basis by means of in situ surveys provided by the Ministry of the Ecological Transition and the Demographic Challenge of the Government of Spain with a variable precision ranging from 10 to 0.1 m. Four surveys are available since 2015: May 2016, September 2019, September 2021, and August 2022. The topographic surveys cover the beach foreshore and backshore, including the inter-tidal area, berm, and dry beach, up to the toe of the dune or seawall. The survey dated September 2021 also covers the dune seaward slope and crest. From these topographic surveys, the shape of the beach profile is extracted along transects placed in the center of polygons (Figure 7). The vertical reference level for these topographic surveys (chart datum of Avilés Port) is located 274 cm below the local mean sea level. Other vertical references, such as the highest astronomical tide, mean high water, mean low water, and the lowest astronomical tide, are shown in Figure 8 with results of the topographic surveys for beach profile No. 6 as an example, along with the window that indicates where SAR-SLs are identified.
- Seasonal changes, based on the correlation between the time series of SAR-SL position (distance from the baseline) and local hydrodynamics. Time series of wave parameters, tides, and surge levels are obtained from the databases Global Ocean Waves [39], Global Ocean Tides [40], and Global Ocean Surges [41], respectively (see time series in Figure A1). Regarding waves, the Global Ocean Waves dataset consists of hindcast data generated with the WaveWatch III numerical model. In the study area, the dataset spans from 1979 to 2021 with a temporal resolution of one hour and a spatial resolution of 0.25 degrees. Regarding the astronomical tide, the Global Ocean Tides provides hourly time series of astronomical tides with global coverage and a spatial resolution of 0.25 degrees. Astronomical tides are generated from the harmonic constants derived from the TPXO global tide model in its different versions developed by Oregon State

University. As for the storm surge, the Global Ocean Surges dataset is a hindcast storm surge dataset generated with the Regional Ocean Model System, which is a three-dimensional oceanic model that solves the Reynolds-averaged Navier–Stokes equations using the Boussinesq approximation. In the study area, the dataset spans from 1985 to 2020 with a temporal resolution of one hour and a spatial resolution of 0.08 degrees.

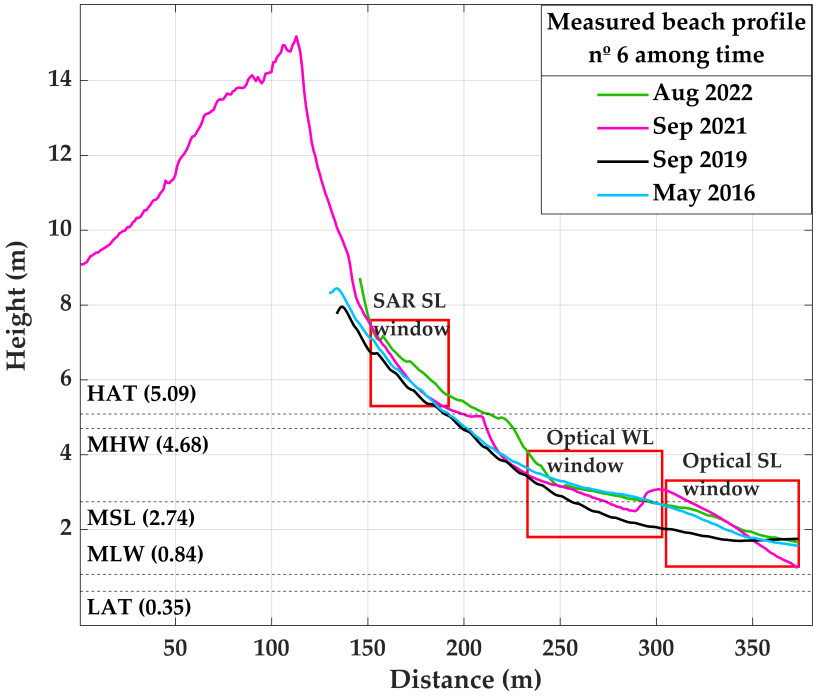

Figure 8. Subaerial and inter-tidal beach profile for Salinas beach from in situ surveys (profile No. 6). The horizontal distance is referenced to the baseline in Figure 7 (HAT is the high astronomical tide; MHW is the mean high water; MSL is the mean sea level; MLW is the mean low water; and LAT is the low astronomical tide).

Additionally, to compare the results that we can obtain from SAR and optical sensors, satellite-derived shorelines (WLs) from S2 images are obtained with the CoastSat tool [42]. The water lines represent the water–sand interface at the moment in which the image was taken. After a visual inspection to remove lines located outside the inter-tidal area, 169 WLs were kept between 2015 and 2022. The position of the shorelines from optical images was obtained as the distance from the baseline in the 61 beach profiles in Figure 7. CoastSat WLs were transformed into datum-based SLs using the total water level (TWL) at the moment in which the image was taken and the beach slope from the topographic surveys to project the WL horizontal position onto the mean low water (MLW) datum (84 cm above the chart datum). Figure 8 shows the windows where CoastSat WLs and datum-based CoastSat SLs are located across beach profile No. 6 as an example.

Finally, the ability of these optical CoastSat WLs and SLs to detect morphological changes in the beach profile at the same two timescales (inter-annual and seasonal) is assessed. However, here, the correction to derive SLs from CoastSat WLs could only be applied before the year 2021 due to the available hydrodynamic data (TWL).

2.5.3. Start Bay

For this study site, we are interested in gaining a better understanding of how much of the tidal range is captured by SAR-SLs and if this dataset and metrics of change can capture the beach rotation observed at Start Bay. To address these questions, we started by visualizing the satellite-derived SLs individually and at different scales. This allowed

the overall characteristics of the lines to be assessed, including their completeness and the presence of any spurious lines, loops, or gaps. The lines were visualized over publicly available high-resolution aerial and satellite optical imagery, allowing for an assessment of where they accurately captured the shoreline and where there were issues. We used Quantum Geographical Information System software (QGIS; version 3.28.0-Firenze) for visualization and analysis. For this study, we used the high-resolution 30 cm imagery layer provided by ArcGIS online services via World Imagery (MapServer), available at https://server.arcgisonline.com/arcgis/rest/services/World_Imagery/MapServer/3 (accessed on 6 December 2023). World Imagery provides satellite and aerial imagery at one-meter or better resolution in many parts of the world and lower-resolution satellite imagery worldwide. The map includes 15 m TerraColor imagery at small and mid-scales (∼1:591 M down to ∼1:288 k) for the world. The map features Maxar imagery at 0.3 m resolution for selected metropolitan areas around the world, 0.5 m resolution across the United States and parts of Western Europe, and 1 m resolution imagery across the rest of the world. In addition to commercial sources, the World Imagery map features high-resolution aerial photography provided by the GIS User Community. This imagery ranges from 0.3 m to 0.03 m in resolution (down to ∼1:280 in selected communities). For more information on this map, including the terms of use, visit ArcGIS online (available at http://goto.arcgisonline.com/maps/World_Imagery, accessed on 6 December 2023).

To address the question regarding how much of the tidal range is captured by the SAR dataset at Start Bay, we used astronomical tide model POLTIPS3 tidal prediction software (POLTIPS-3; Standard version 3.9.02/21 Standard) [43], which allows us to compute the astronomical tide around 700 UK ports using harmonic components provided by the National Oceanographic Centre. The tide elevations (daily high and low tides) are computed at Start Point relative to the chart datum and are converted to the ordnance datum using Vertical Offshore Reference Frames software (VORF; version 2.11) [44]. The datum used for the British mainland (and some of the closer offshore islands) is called Ordnance Datum (Newlyn), as it is based on the average value of the mean sea level at Newlyn for the six-year period from 1915 to 1921. Due to the subsequent rise in mean sea level, this datum is now about 0.2 m below mean sea level at Newlyn. The tide level at the time when the satellite data were collected is obtained through linear interpolation of the daily high and low tides using the date and time (in coordinated universal time).

To better understand the location of the SAR-SLs and the ability to capture beach rotation, we used high-resolution digital terrain models (DTMs) publicly available via the National Network of Regional Coastal Monitoring Programmes of England (available at https://coastalmonitoring.org/ (accessed on 6 December 2023)). We used the filtered LiDAR data in ASCII format at 1 m resolution for the years 2016, 2018, and 2021, as shown in Figure A2 in Appendix A. Each tile is 5 × 5 km and aligned to the Ordnance Survey National Grid. Each pixel represents 1 m spatial resolution on the ground, and elevations are referenced to Ordnance Datum Newlyn. Errors in elevation DTM values are of the order of ±0.5 m. We used the QGIS plugin named "Value Tool" to extract the elevation along each SL from the DTM closest in time to the time of the SAR data collection. We used the QGIS raster calculator to obtain the digital elevation model of difference (DoD) that represents the elevation difference between two time-stamped DTMs. The DoD is calculated by subtracting the elevation at each pixel of the most recent DTM and the elevation of the oldest DTM, resulting in negative values indicating losses in elevation or erosion and positive values indicating gains in elevation or accretion. Visualizing the SAR-SLs over the DTMs and the DoD allows us to assess if they capture different elevations and areas of change.

3. Results

3.1. Bull Island

Figure 9 illustrates an overview of the SAR-SLs extracted for Bull Island. They were generated by processing the available SAR images between June 2016 and March 2022.

As RL, the high-water-mark shoreline produced by Ordnance Survey Ireland (https://www.geohive.ie/pages/data (accessed on 6 December 2023)) was used. Along the RL, 93 polygons were created, and for each of them, SAR CRs were produced in order to validate it "quantitatively". The speckle effect is minimal along the front beach (Figure 9a). The majority of the SLs appear to be well concentrated and unaffected by sea conditions, suggesting a relatively calm environment during data acquisition. Figure 9b illustrates the points selected for the annual SL CR after applying a minimal filter (heatmap >0.175%) and the GMD technique. Considering the flat beach geometry, the authors note that there is good overall agreement between the results obtained from SAR ASC and DESC tracks. The geometry distortions (shadows/layovers) do not appear to have a noticeable effect on the SLs. This results in the SLs tending to overlap with one another. The slight differences observed are attributed to variations in the number of SAR images available. Bull Island is not covered equally from ASC (759) and DESC (386) tracks, which may lead to minimal differences in certain polygons.

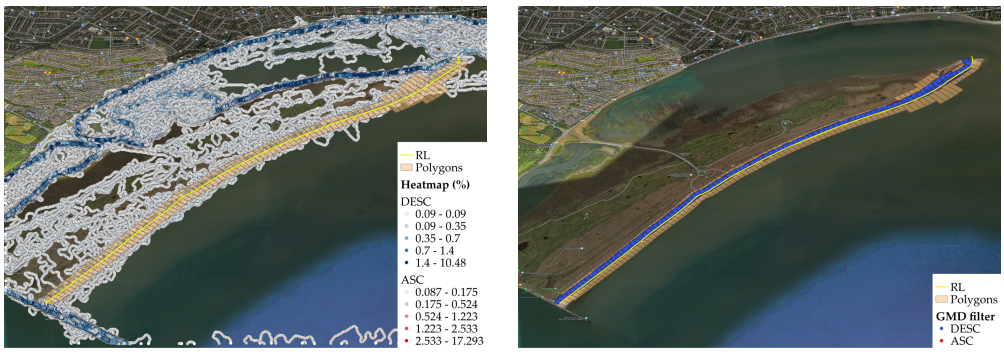

(**a**) (**b**)

Figure 9. SLs produced for Bull Island including both ASC and DESC tracks (**a**). Filtering applied to the scene and points selected to produce time series and change rate (**b**). Source of aerial imagery: Google, ©2023 Maxar Technologies.

The Bull Island shoreline consists of 5 km of low-lying sand dunes. The shoreline change shows a gradual transition from advancing shoreline in the southern part to receding in the northern end. The central part lies within the stability range. The overall trend is accretion, covering 2/3 of the shoreline. However, the average shoreline change rate is negative (receding), −0.54 m/year, as the northern part shows high erosion values up to −9.95 m/year (Table 4).

Table 4. Shoreline annual CR stats for SAR ASC, SAR DESC, and DSAS vegetation line (VL DSAS).

SL Annual CRs	N	Mean	Max	Min	Advancing	Receding
SAR ASC	93	−0.95	−11.72	1.36	47/93	46/93
SAR DESC	93	−1.18	−10.71	1.46	40/93	53/93
VL DSAS	93	−0.54	−9.95	3.51	62/93	31/93

Overall, there is a high degree of alignment between the CRs derived from DSAS and SAR shorelines. This is confirmed in the visual inspection of the profiles (Figure 10) and the strong correlation coefficients ($R^2 > 0.9$) between the two datasets (Table 5). In general, SAR annual SL CRs are lower than the DSAS counterparts, in both average values and coverage. Regarding the mean rates, the SAR CRs are lower than the DSAS rates (∼0.5 m/year) and display larger receding rates. The receding shoreline extent is larger in both SAR passes (ASC/DESC) when compared with DSAS rates.

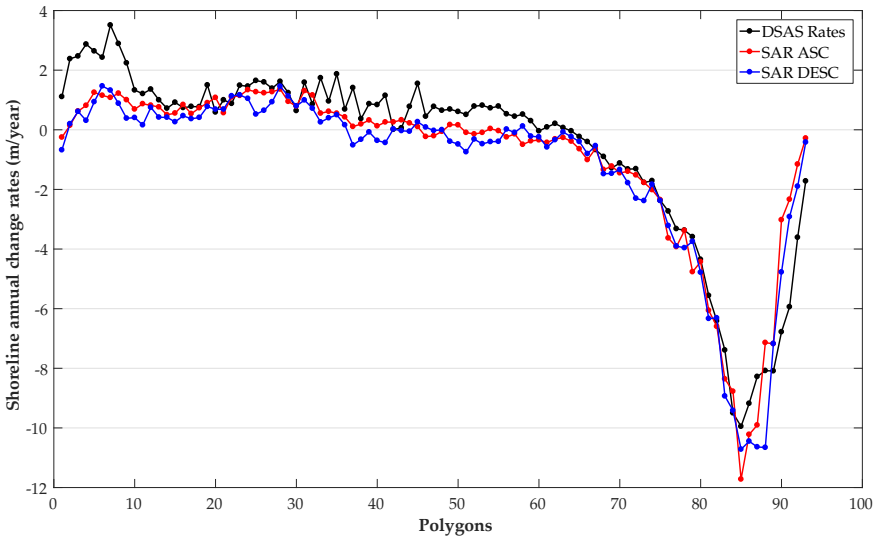

Figure 10. Profile format comparison between DSAS and SAR CRs. Annual SL CRs were calculated for each polygon using the two methodologies described previously. The profiles show very strong agreement between SAR ASC and DESC tracks and strong agreement between DSAS and SAR change rates.

Table 5. Shoreline annual CR linear correlation indices among SAR ASC, SAR DESC, and DSAS VL.

	N	R^2	MAE	MAE (WLR < 0)	MAE (WLR > 0)
SAR ASC/ SAR DESC	93	0.97	0.37	-	-
VL DSAS/ SAR ASC	93	0.90	0.75	0.83	0.70
VL DSAS/ SAR DESC	93	0.92	0.84	0.80	0.86

3.2. Salinas Beach

The SAR-SLs in Salinas are extracted from 773 SAR images (ASC) and 726 images (DESC) acquired between January 2015 and September 2023. The RL is obtained using an innovative tool based on the Open Street Map (OSM) catalog, showing much more agreement with the Google Earth images [45]. The beach area is partitioned into 61 polygons, each spanning a width of 50 m. In contrast to the previous location, Salinas presents a complex situation (depicted in Figure 11). The consequence of the speckle due to the sea conditions is quite evident, as SL points span over a wider area (extending over 800 m from the RL, as shown in Figure 11a). This poses a challenge to discerning the primary concentrations of SLs. Heatmap filtering (>0.2%) allows for a reduction in a significant part of the noise. The SLs obtained after applying the GMD filter are displayed in Figure 11b.

Although there is an overlap between the ASC and DESC points, the lengths of certain polygons (length associated to the main SL concentration) exhibit disparities attributable to the scene's geometry. Along the eastern, urban part of the beach, ASC points are located more inland compared with DESC points, whereas the opposite occurs in the western part. Notably, geometry-related distortions such as shadows and layovers considerably impact the representation of SLs at this location. The longshore migration of crescentic bars in the inter-tidal area of Salinas beach complicates the analysis of the evolution of topographic contour lines, and consequently, it is difficult to relate the changes in the shoreline planform shape due to erosional or accretional processes over time. These complex 3D morphologies dominate most of Salinas beach (profiles No. 10 to No. 61 in Figure 12). However, on the western and eastern boundaries of the beach, where coastal morphodynamics are

constrained due to the rocky headland and inlet groin, respectively, most changes in the shoreline position can be attributed to a net accumulation or loss of sediments in the beach profile.

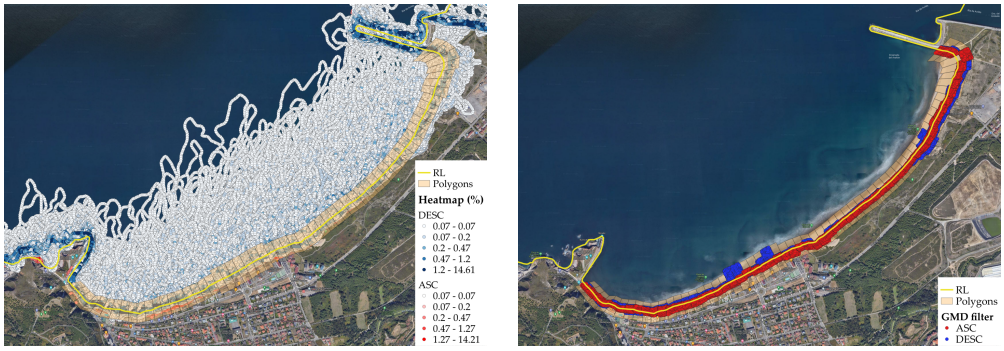

(**a**) (**b**)

Figure 11. SLs produced for Salinas including both ASC and DESC tracks (**a**). Filtering applied to the scene and points selected to produce time series (**b**). Source of aerial imagery: Google, ©2023 Maxar Technologies.

Figure 12. Topographic contour lines in Salinas beach for 2022 (MLW = mean low water, MSL = mean sea level and MHW = mean high water). The numbers indicate the beach profiles in the scene. Source of aerial imagery: Esri, World Imagery Metadata.

All analyses for Salinas beach are associated with changes observed in the eastern boundary of the beach (profiles No. 1 to No. 9 in Figure 12). The orientation of beach profiles No. 1 to No. 3 is significantly oblique with respect to the average orientation of Salinas beach, thus profile No. 6 is selected as the central transect of the eastern boundary, and it is considered representative of this part of the beach. After filtering, for this profile, from all the available SAR images, 684 ASC and 630 DESC SL positions (d_M) are used to assess both the seasonal and inter-annual migration of the SAR-SL in the cross-shore direction.

3.2.1. Seasonality in Salinas SAR-SL

The SAR-SL time series shows a seasonal pattern in Salinas beach, according to which the SAR-SL migrates inland during winter and returns to a more accreted position in summer (Figure 13).

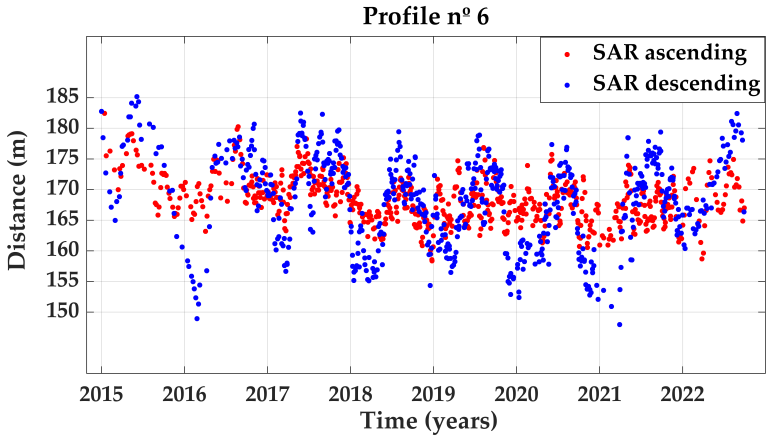

Figure 13. Time series of SAR-SL distance from the baseline in Salinas beach.

The available in situ topographic surveys (four in seven years) are not enough to study the intra-annual behavior of the beach profile; therefore, validation of the seasonal morphodynamic pattern based on the available ground-truth data from topographic surveys in Salinas is not possible. Instead, in this assessment, the correlation between SAR time-series SLs and local hydrodynamics is analyzed. To achieve this, time series of the TWL are calculated from the available oceanographic data (see Section 2.5.2) as an aggregation of the astronomical tide, storm surge, and the estimated wave run-up exceeded by only 2% of the waves within the sea state [46]. A simple moving average of the TWL is represented in Figure A3 in Appendix A based on a 24 h sampling window to reduce the impact of the semidiurnal astronomical tide (with 5 m of spring tidal range in Salinas) in the inter-annual TWL time series.

Figure 14 shows that most SAR-SL distances under a threshold defined as the highest annual minimum (corresponding to the year 2017) take place within the time window in which the 95% percentile of the TWL is exceeded by the TWL moving average time series.

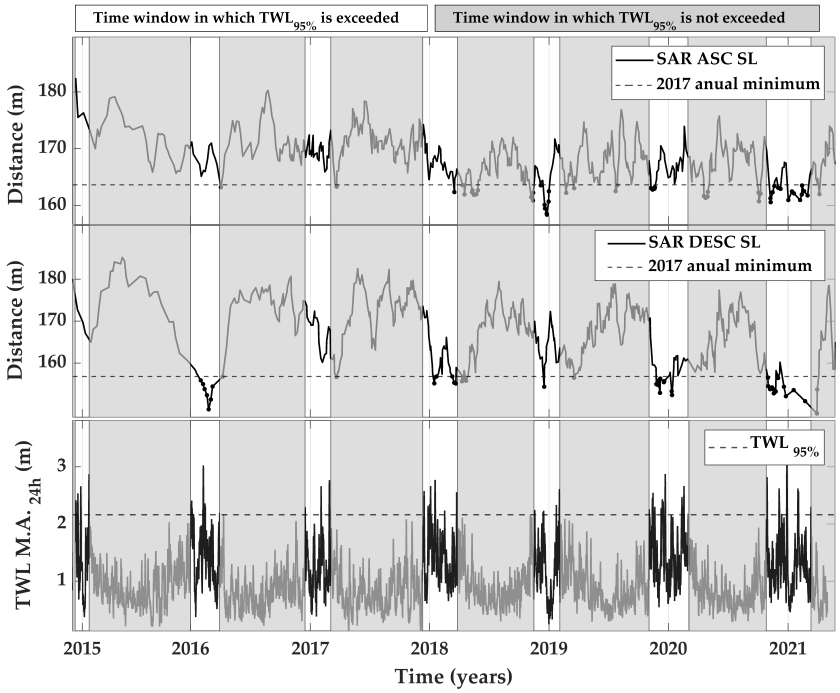

Figure 14. SAR-SL distance from the baseline in Salinas beach (**top** and **middle** panels); TWL moving average (TWL M.A.; **bottom** panel).

The qualitative correlation detected between the highest values of the TWL and the most retreated SAR-SL positions is stronger for SAR DESC. SAR DESC also shows a

stronger seasonal pattern, which consists of a landward migration of the SL during winter and a seaward migration during summer. This agrees with the theoretical behavior of the equilibrium beach profile, which is expected to move seaward due to low-energy waves in summer, while it is expected to move landward during the energetic swell in winter seasons.

3.2.2. Inter-Annual Changes in Salinas SAR-SL

Following the seasonal assessment, only SAR DESC tracks are considered in the analysis of the inter-annual behavior of SAR-SLs to reduce the uncertainty associated with the variability in the SAR signal in the input data. The SAR DESC SL positions are detected as the horizontal distances from the baseline. The distances range between 156.7 m and 182.4 m, which corresponds to an area located above the HAT (5.09 m) in the upper beach profile. In this area, the following morphodynamic behaviors are observed (in a qualitative way) in the four in situ topographic surveys (see Figure 15, upper panel):

- In May 2016, the beach profile was in an intermediate position.
- In September 2019, the beach profile migrated inland, showing maximum beach erosion.
- In September 2021, the beach profile came back to an intermediate position, like in May 2016.
- In August 2022, the beach profile migrated seaward, showing maximum beach accretion.

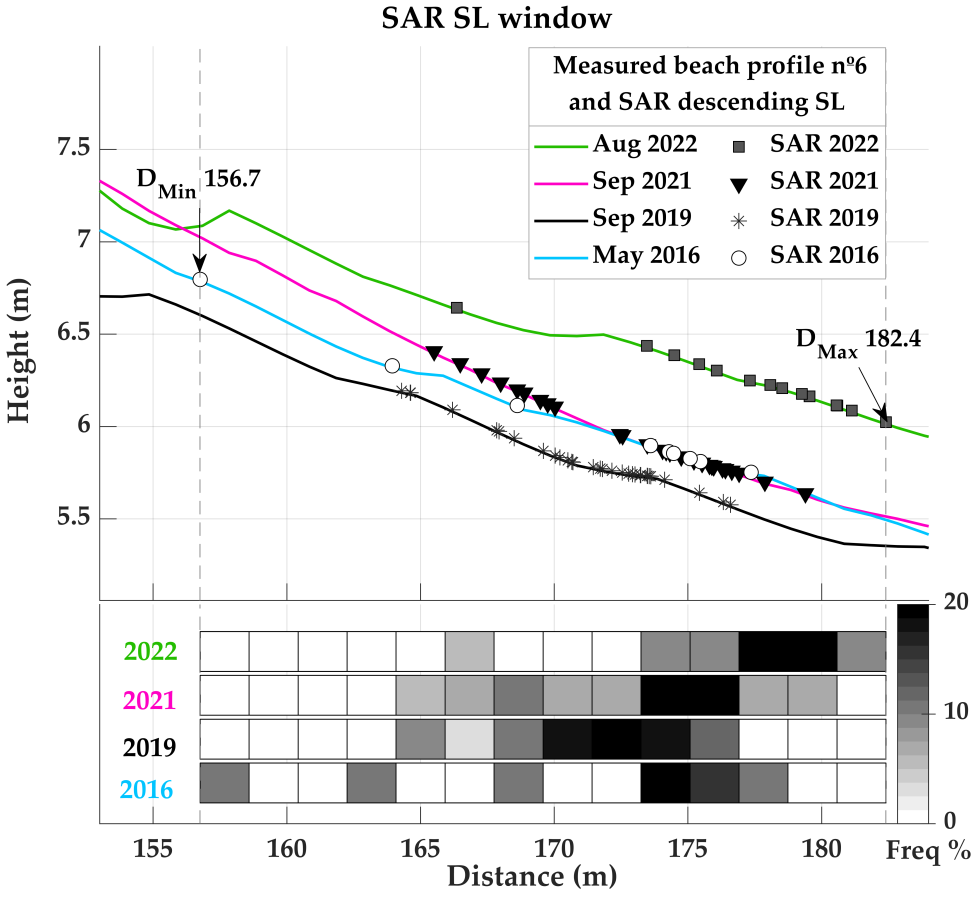

Figure 15. Measured beach profile (No. 6) and SAR-SL distance from the baseline in Salinas beach (**top** panel); heatmaps of concentration of SAR DESC SLs across the beach profile (**bottom** panel).

To compare the observed changes in the beach profile with changes in the SAR signal, all SAR DESC SLs detected within the period of ±1 month from the survey month are selected. The SAR DESC SL horizontal positions with respect to the baseline during these 3 months are represented in heatmaps that show the concentration of SAR DESC SLs in

14 sections of the upper beach profile (see Figure 15, lower panel). The same behavior observed in in situ data is present in the results of SAR DESC SLs (see concentration over 20% in the heatmaps in Figure 15): the SAR DESC SLs in April–June 2016 and August–October 2021 are in intermediate positions; the SAR DESC SLs in August–October 2019 are in the most retreated position; and the SAR-SLs in July–September 2022 are in the most advanced position.

3.2.3. Change Detection from Optical WLs in Salinas

The available number of optical (CoastSat) WLs is significantly lower than the number of available SAR DESC SLs for the same period (see Table 6), which hampers the ability of CoastSat WLs to detect intra-annual morphological changes. No seasonal pattern is observed in the CoastSat WLs, nor in the datum-based CoastSat SLs projected onto the MLW.

Table 6. Available SAR DESC SLs and CoastSat WLs within a 3-month time frame around the date of the in situ topographic surveys.

Time Frame	SAR DESC SL	CoastSat WL
April–June 2016	9	7
August–October 2019	31	8
August–October 2021	29	3
July–September 2022	14	10
Total No. of records	83	28

As for the inter-annual changes in the beach profile, in the inter-tidal area where the CoastSat WLs are detected, the following qualitative morphodynamic behaviors are observed in the four in situ topographic surveys (see Figure 16a, upper panel):

- In May 2016, the beach profile was in the most advanced position, showing maximum beach accretion.
- In September 2019, the beach profile migrated inland, showing maximum beach erosion.
- In September 2021, the beach profile migrated seaward to an intermediate position.
- In August 2022, the beach profile migrated further seaward, showing maximum beach accretion, like in May 2016.

Similar to the previous analysis, the horizontal distances from the baseline of the CoastSat WLs detected during 3 months around the date of the in situ topographic survey are represented in the heatmaps that show the concentration of CoastSat WLs in 14 sections of the inter-tidal beach profile (see Figure 16a, lower panel). Changes over time in the area with the highest concentration of CoastSat WLs in each period (over 20%) do not show any erosional or accretional behavior. The same is observed when using the CoastSat SLs corrected to the MLW datum. The correction from WLs to SLs, commonly applied to improve coastal change detection from optical images, did not reduce the dispersion of the CoastSat SLs across the beach profile in comparison to the CoastSat WLs (see Figure 16b).

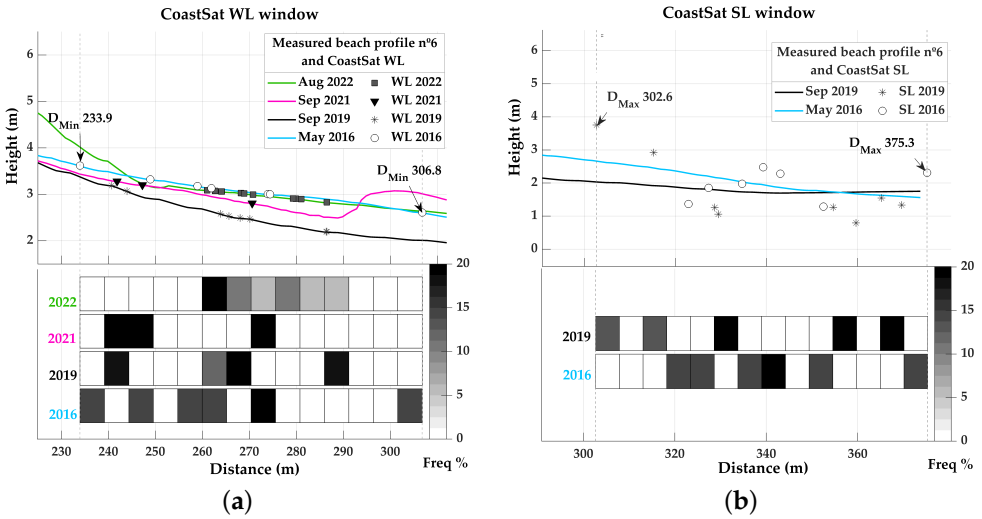

Figure 16. Measured beach profile (No. 6) and CoastSat WL distance from the baseline in Salinas beach (top panel **a**); heatmaps of concentration of CoastSat WLs across the beach profile (bottom panel **a**). Measured beach profile (No. 6) and CoastSat SL distance from the baseline in Salinas beach (top panel **b**); heatmaps of concentration of CoastSat SLs across the beach profile (bottom panel **b**).

3.3. Start Bay

Figure A4 in Appendix A shows the location of all the SLs derived from ASC (701 lines) and DESC (701 lines) orbits at the Start Bay study site between the years 2015 and 2021. The RL used is the same datum-based tideline used by [15], which represents the contour at −1.3 m elevation relative to the ordnance datum extracted from the 2019 SurfZone DEM. SAR-SLs seem able to delineate the relatively homogeneous and rectilinear gravel beach, the very irregular rocky outcrops, and the large lagoon. A visual inspection of SAR-SLs indicates that they are predominately continuous with few spurious lines. In places, the SL appears as spurious irregular segments, with this being most appreciable for ASC SLs at the northern and southern ends of the large embayment and for the DESC SLs at the seaside and center of the large embayment. A zoomed-in view of different regions showing all lines (ASC and DESC SLs) in bulk reveals that there is not a clear tendency of lines extracted from one orbit to appear systematically landward or seaward with respect to the other.

A zoomed-in inspection of individual SLs reveals that the SLs are wiggly at places, but this did not appear to be too detrimental to the understanding of the line as a water–land approximate interface. The width of the envelope of all SLs in the enclosed lagoon area is of the order of 30 m and appreciable smaller than along the open coast, where it is of the order of 150 m. We noticed that only a subset, six and eleven SLs for ASC and DESC, respectively, of the seven-hundred and one SLs mapped the lagoon as part of the open coast, suggesting that the barrier might have been breached. The dates on which the lagoon was mapped for the ASC SLs are all different from those the DESC SLs (see Table 7).

Table 7. Dates of DTM collection, and dates and time of ASC and DESC SLs used for the analysis. It is also indicated if the astronomical tide was ascending, descending, or at high tide at the time of satellite data collection.

DTM Collection Date	SL Collection Date, Time, and Astronomical Tidal Level	
	Ascending SLs	Descending SLs
10 March 2016	11 March 2016 18:05:17 ↑ 1.1 m	08 March 2016 06:31:08 ↓ 1.5 m
12 September 2018	10 September 2018 17:56:36 ↑ 2.4 m	† 12 September 2018 06:31:08 ↑ 1.7 m
19 September 2020	17 September 2020 17:57:42 ↑↓ 2.7 m	† 19 September 2020 06:31:50 ↑ 2.2 m

† Collection dates of DTMs and SLs within less than 24 h difference; ↑ ascending tide; ↓ descending tide; ↑↓ high tide.

Figure 17 shows the summary statistics of the astronomical daily high and low tide elevation at Start Bay between the years 2015 and 2021, together with the elevation at the time when the satellite data were collected grouped into ASC and DESC tracks. All tide elevations are shown relative to Ordnance Datum Newlyn (ODN). The passing times are between 17:57 and 18:05 UTC (coordinated universal time) for the ASC tracks and between 6:23 and 6:31 UTC for the DESC tracks. At these collection times, the median tide elevations seen by the satellites are 0.5 m and 0.6 m for the ASC and DESC tracks, respectively, which are higher than the median value for the site of 0.3 m. The minimum astronomical tide elevation at the site is −2.6 m, which is lower than the minimum elevation at the time of satellite data collection, which is −1.0 m for the ASC tracks and −1.1 m for the DESC tracks. The range of tide elevations, calculated here as the difference between the maximum and the minimum elevation, is 5.6 m, while the range of elevations captured by the satellite is 3.8 m. These results indicate that satellite observation at this study site only captures about 68% of the astronomical tide elevation range of the daily high and low values and is 0.2 m to 0.3 m biased towards high elevation.

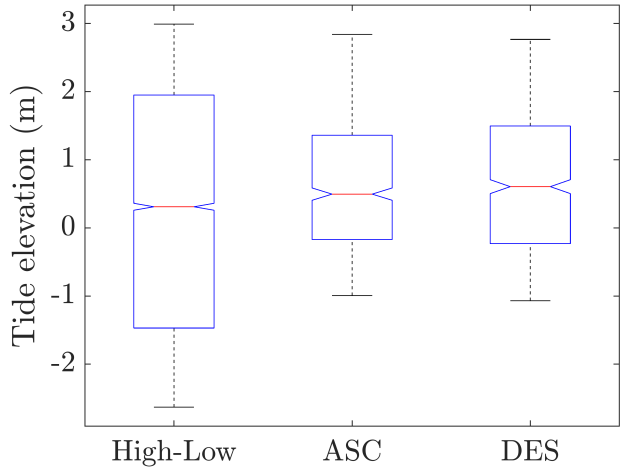

Figure 17. Astronomical tide elevation at Start Bay study site for the years 2015 to 2021 from the daily high and low tides, and subsets of when ASC and DESC images were taken. Elevations are obtained using POLTIPS software at the Start Point tide gauge station and refer to Ordnance Datum Newlyn. BGS ©UKRI.

Table 7 shows the collection dates of the DTMs used for this analysis and the shorelines closest in time derived from the ASC and DESC satellite tracks. Out of the six total SLs (three ASC and three DESC), only two of the DESC SLs were collected on the same day of the DTM data collection on the 12th September 2018 and the 19th September of 2020, both at the time when the tide was rising. None of the ASC SLs were collected on the same day of DTM collection but within ±2 days of DTM data collection and all of them during ASC tides, with the SLs being collected on the 17th September 2020 two minutes before high tide, which was at 17:59 UTC. The only SL collected during descending tide was on the 8th of March 2016 and close to the daily high tide, which was at 05:20 UTC. The astronomical tide elevation at the time of these SL collection operations varied from 1.1 m to 2.7 m.

Figure A5 in Appendix A shows the location of the ASC and DESC SLs over the DTMs used for the elevation analysis for Start Bay, and Table 8 shows the main stats of the terrain elevation values along the SLs. The seaward limit of the DTMs is constrained by the lower sea water level at the time of data collection, and most of the SLs are located within the DTM spatial domain, except for some segments of the SLs for the year 2020 and most appreciably for the DESC SLs in the year 2020. The mean number of points with no nan-values (e.g., line is mapped within DTM spatial domain) for all the SLs of the two types in the year 2020 is of the order of 8000 points, while for the years 2016 and 2018, it is of the order of 10,000 points. The minimum, maximum, mean, and median terrain elevations

for all six lines are -2.4 ± 0.2 m and 37.9 ± 8.8 m, 3.8 ± 0.9 m and 3.0 ± 0.5 m, respectively. The points where we observe the largest elevations are located in places where there is a high cliff with a steep slope and a narrow inter-tidal area. Both the mean and the median elevation values are higher than the astronomical tide levels shown in Table 8. Surprisingly, the mean and median terrain elevation are at the minimum on the 17 September 2020, which is the date with the largest astronomical tide level. The lagoon has been mapped as part of the open coast by the only SL captured during descending tide on 08 March 2016, and there is no evidence of breaching in the DTM closest to this date.

Table 8. Main stats (count of non-nan values, minimum, maximum, mean, standard deviation, and median) of the terrain elevation values along the SLs extracted from the DTMs for Start Bay. Elevation values refer to OD Newlyn.

SL Name	Count	Min (m)	Max (m)	Mean (m)	Std (m)	Median (m)
ASC 11 March 2016 ↑	10324	−2.7	26.5	3.3	3.5	2.8
ASC 10 September 2018 ↑	10311	−2.1	50.0	4.2	6.3	3.1
ASC 17 September 2020 ↑↓	8693	−2.6	29.5	2.3	3.2	2.4
DESC 08 March 2016 ↓	10826	−2.5	44.0	4.6	6.5	3.2
† DESC 12 September 2018 ↑	10147	−2.2	40.6	4.6	5.5	3.8
† DESC 19 September 2020 ↑	7791	−2.7	36.8	3.5	5.3	2.8

† Collection dates of DTMs and SLs within less than 24 h difference; ↑ascending tide; ↓ descending tide; ↑↓ high tide.

Figure 18 shows the changes observed at the Blackpool Sands embayment in Start Bay between 2016 and 2018 and the closest SAR-SLs to the observed DTMs together with the metrics of change obtained using all lines for the study period between 2015 and 2021.

Blackpool sands is a small embayment located at the north end of Start Bay that shows how the beach rotates: sediment eroded from one end is deposited at the other end of the embayment, with a nodal point of no elevation change close to the center of the embayment. Figure 18a shows the SAR-derived shorelines on top of the DoD obtained from subtracting the elevations observed in 2016 from the elevations observed in 2018, so negative and positive elevation differences represent erosion and accretion, respectively. The elevation differences are well within ± 1.5 m, suggesting that sediment eroded from the northern end has been deposited in the southern end of the embayment (e.g., counterclockwise beach rotation). We notice that most of the elevation changes are in the upper swash zone, while the SAR-derived SLs are mostly located in the upper backshore and far from the main area of vertical change. The filtered shoreline points used to obtain the metrics of change from all the satellite observations available are shown in Figure 18b. More than 70% of the filtered shoreline locations are outside the area of appreciable vertical change except for points located on the northern end of the embayment. When using all the SAR data available to calculate the annual recession rate, we observe that the rotation is somehow captured as shown in Figure 18a,d, where eroding polygons and accreting polygons dominate different ends of the embayment. Polygons where annual change rate is within ± 0.5 m are not shown (e.g., transparent polygons), and as expected, the central part of the embayment is within these neutral polygons. We also notice that the direction of change observed in the DoD between 2016 and 2018 is opposite to the direction of change obtained when using all observations between 2015 and 2021: beach rotation is counterclockwise for the period 2016-2018 and clockwise for the period 2015 to 2021.

Figure 19 shows the annual CRF for the entire Start Bay area obtained from all the SAR observations for the time between years 2015 and 2021, and as a visual reference, we also show the DoD between 2016 and 2018.

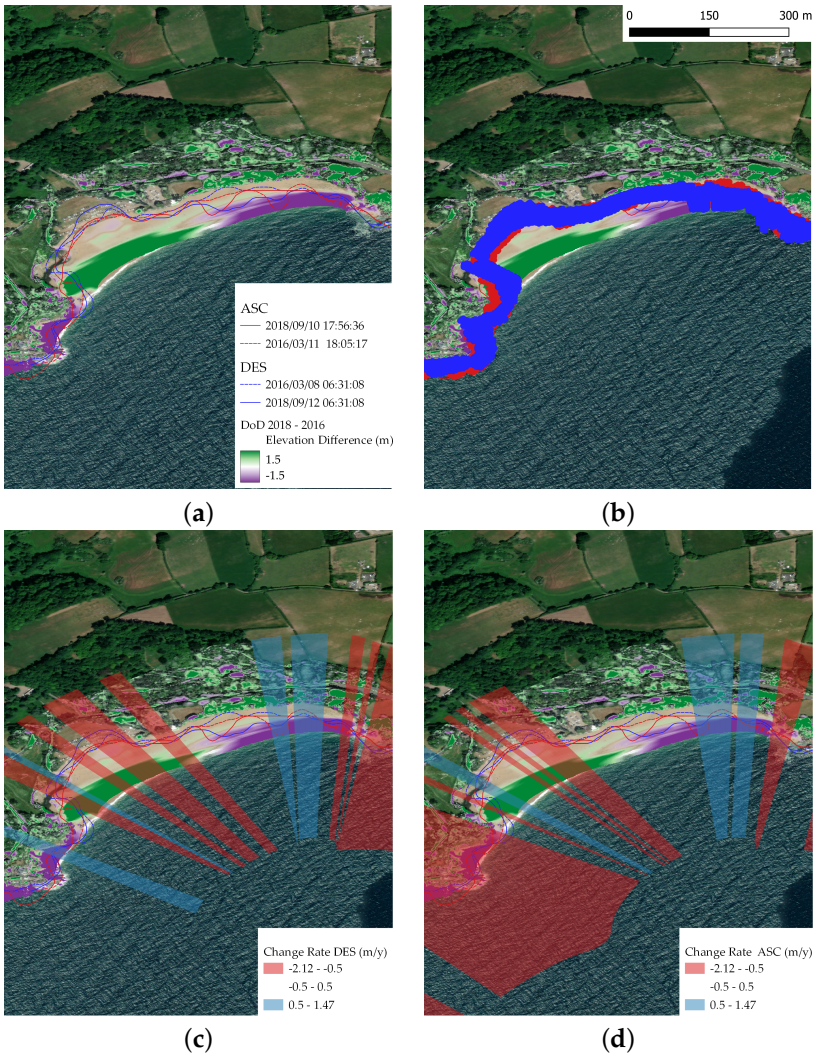

Figure 18. Qualitative assessment of SAR shorelines detecting beach rotation at Blackpool Sands embayment in Start Bay. (**a**) Shorelines from ascending and descending orbits for the years 2016 and 2018 shown on top of the digital elevation model of difference. (**b**) Points filtered out from the shorelines obtained from ASC (red points) and DESC (blue points) that are used to calculate the annual recession rate using all data available for the period 2016 to 2021. (**c**,**d**) Polygons showing the annual change rate obtained from DESC and ASC filtered points, respectively. Source of aerial imagery: Esri, Maxar, GeoEye, Earthstar Geographics, CNES/Airbus DS, USDA, USGS, AeroGRID, IGN, and the GIS User Community (v10.6). BGS ©UKRI.

The histograms show how the mean annual change rate is negative for both ASC and DESC SLs but of different values -0.6 m/year and -0.2 m/year, respectively. This is due to most of the metrics of change obtained from the DESC SLs resulting in neutral CRs (e.g., within ± 0.5 m/year), unlike for metrics of change obtained from the ASC SLs. The southern end of Start Bay is dominated by rocky outcrops that change very little in elevation over time. This stability seems to be better captured by the metrics of change derived from DESC SLs, which show neutral (± 0.5 m/year) annual change rate at the southern end, while the metrics of change derived from ASC SLs show erosive annual CRs larger than -0.5 m/year.

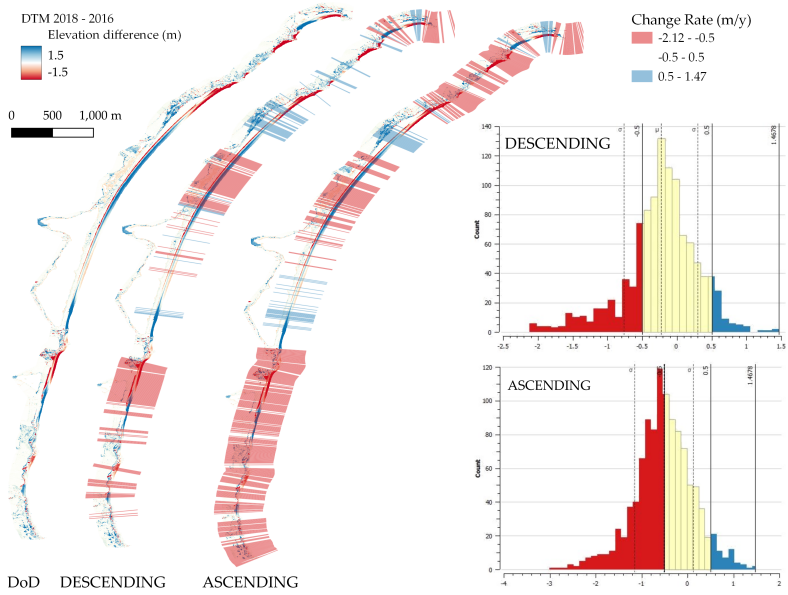

Figure 19. Annual CRs derived from ASC and DESC shorelines at Start Bay shown on top of the 2016–2018 digital elevation model of difference (DoD). Histograms show the annual rate value distribution in three categories (erosive in red, neutral in yellow, and accretive in blue). Neutral changes (yellow bins) are shown as transparent polygons in the maps for clarity. BGS ©UKRI.

4. Discussion

The results presented here highlight the potential of applying SAR images for analyzing changes in coastal morphology and raise questions that will benefit from further research. SAR-SL time series (e.g., from S1) enable between 10 and 25 times more observations for a given time period when compared with those derived from optical sensors (e.g., S2; see Table 1). This advantage arises from SAR's independence from cloud cover and day light [47], making SAR data powerful information to detect short-term changes, such as those that occur during severe storms. Such high-frequency shoreline time series would also allow for defining other coastline indicators. For example, some authors highlighted the advantage of using probabilistic shorelines instead of deterministic ones when assessing coastal dynamics [47,48]. This kind of SL indicators allow for dealing with the uncertainty in shoreline detection by estimating a probabilistic SL position based on several measurements.

Through the validation analysis carried out in the three tidal beaches studied here, we explored the ability of SAR to detect coastal changes in sites that represent a challenge for typical satellite monitoring techniques, and the results demonstrated a coherence between SAR-SLs and the ground-truth data. We have shown how the rates of change obtained from SAR-SLs agree with the change rates derived from the vegetation lines in Bull Island; the SAR-SLs in Salinas seem to be mapping changes in the upper shoreface and are able to capture the beach rotation observed in Start Bay. However, although SAR-SL time series were correlated to the changes observed in the ground (CRs, extreme TWL, and beach rotation), our findings also highlighted that SL detection using this technology is a complex and multifaceted task. This complexity arises from the dependence of SAR-SL detection on a set of variables, including but not limited to the relationship between the satellite orbit (ASC or DESC) and the geometry of the observed coastal scene, the sea conditions at the moment of SAR detection, the dielectric constant properties of sand, and the fluctuating tidal level. Each of these factors has an impact on the SAR signal and makes SAR-SL characterization a challenge. For example, the complexity of the SAR signal makes it difficult to define what is being detected as shoreline at each site, as local environmental conditions may play a significant role in this task [47]. Local characteristics may also result in difference in shoreline detection from ascending and descending orbits, and it is crucial

to identify which data should be used at each site to obtain reliable results regarding coastal changes. Based on the results we obtained from the three study sites, in the following, we discuss some of the site-specific aspects that may affect SAR-SL detection, highlighting the points that still need to be further explored to improve shoreline change analysis based on SAR techniques.

4.1. The Influence of Met-Ocean Conditions

One of the constraints within SAR satellite systems is the influence of sea conditions, which introduce speckle noise, thereby compromising the image quality and the accuracy of the SLs derived from SAR. The issue arises from the inherent roughness of sea surfaces, causing radar signal to scatter in various directions [49]. This scattering behavior hinges on several factors, such as ocean wave conditions and wind speed. Consequently, the received radar signal's strength fluctuates due to scattering, leading to the characteristic speckle pattern seen in SAR images. Moreover, sea conditions are not static; they can rapidly change due to factors like wind, tides, and currents. These fluctuations introduce temporal variability in how radar waves interact with the sea surface. Since an SAR system collects multiple radar readings over time, these changing sea conditions across different acquisition instances can contribute to speckle noise. This occurs because they create varying interference patterns in the radar returns. This is the case of Salinas beach, for example. This beach often experiences high-energy sea conditions, and it is exposed to strong winds, resulting in a high amount of speckle. Conversely, both Bull Island and Start Bay are only slightly impacted by such met-oceanographic conditions, resulting in less speckle.

To face this problem, some works have suggested the use of met-ocean data to select those scenes that provide less speckle noise [50]. However, such selection would reduce significantly the number of SAR-SLs obtained in sites where this issue occurs frequently, such as Salinas. In the methodology presented here, the filter based on the heatmap of shorelines allowed for the identifying and selecting of data from areas with high probability of occurrence of shorelines, avoiding the disturbance in areas far from typical SAR-SL detection, such as those where sea surface roughness is strongly affected by waves and wind.

4.2. The Influence of Soil Moisture

Despite the different local settings in the three study sites (cliffs, dunes, vegetation, etc.), SAR-SLs are always detected in the upper part of the beach and far from the inter-tidal zone, which suggests that SAR most likely detects the wet–dry sand boundary. This may be due to the polarization method used in the analysis (VH). When using VH polarization, SAR is likely to detect the interface between wet and dry sand, as the signal shows distinct backscatter signatures according to soil moisture. In this context, the dielectric constant of the material being imaged plays an important role in SAR-SL detection. A dielectric constant is a measure of how a material responds to an electric field, also known as relative permittivity. According to the dielectric constant, the backscatter from radar signals is different, and it allows for the distinguishing of sand from other surfaces, such as vegetation and water bodies. Furthermore, SAR is sensitive to sand moisture, resulting in distinct backscatter signatures between dried and wet sand. Because of the presence of water, dry sand has relatively low moisture content and a low dielectric constant, while wet sand has a high dielectric constant. Wet sand is more efficient in absorbing the SAR signal, resulting in a different backscattered signal response in the SAR image. As a result, wet sand backscatters a weaker signal than dried sand. Although these properties can help to identify the shoreline as the wet–dry interface, it can be an issue in sites where night dew humidifies the sand, affecting SAR-SL detection, as the contrast between the SAR signals from wet and dry sand will not be clear.

Other studies suggest the use of images obtained from other polarization methods to detect shorelines from SAR sensors [51]. Thus, the results obtained here appear to be interesting findings for coastal erosion analysis. Using this configuration (i.e., VH), it is

possible to provide a detailed description of the beach, enabling a better understanding of the erosion and deposition processes along the coast. However, other causes of sand wetting, such as rainfall or morning dew, should be further investigated at the three study sites.

4.3. The Influence of Scene Geometry

Our results revealed discrepancies in shoreline position from ASC and DESC tracks depending on the scene geometry at each site. For example, in Bull Island, where the topography is quite flat, the rates of change obtained from SAR ASC SLs and SAR DESC SLs were very similar, with a correlation of $R^2 > 0.9$. On the other hand, in areas with complex relief and high features in the backshore, such as the cliffs at Start Bay, the discrepancies are evident, with rates of change obtained from DESC and ASC indicating either that a great part of the beach is close to no change ($\pm$0.5 m/year) or that half of the beach is under an erosion process. These differences are linked to the varying angles between the observed scene and the satellite's path during image acquisition along ASC or DESC tracks. During the ascending orbit (south to north), the SAR sensor faces east, while during the descending orbit (north to south), it faces west. This means that the SAR signal reaches the terrain with different incident angles according to the satellite orbit, which affects SAR-SL detection in scenes with complex geometries. The illustration in Figure A6 presents an example of the result of these differences for Start Bay.

In sites where the terrain is flat and devoid of cliffs (Figure A6a), the SLs from ASC (Figure A6b) and DESC (Figure A6c) tracks exhibit congruence (Figure A6d). This is the case of Bull Island, where the change rates observed in SAR-SLs from both ASC and DESC orbits yielded similar results ($R^2 = 0.97$), and both were in accordance with change rates calculated from the vegetation line (DSAS) ($R^2 = 0.90$ for ASC and $R^2 = 0.92$ for DESC) (see also Figure 10). On the other hand, in places with complex geometry, such as cliffs and dunes (Figure A6e), the differences between the results from ASC and DESC increase (as shown in Figure A6h). This is the case of Start Bay. This beach is oriented to the east, and the SAR-SLs from the DESC orbit (Figure A6g) detect the cliff toe better than the ASC orbit (Figure A6f), as the latter is affected by the layover effect and results in SAR-SLs positioned more inland. A similar problem is observed in Salinas, and a noticeable displacement between ASC and DESC is observed due to the presence of dunes, although the effect of the ground geometry on the results is less pronounced (see Figure 13). In this case, SAR-SLs from the DESC orbit are located more inland than SAR-SLs from ASC. Salinas beach is oriented to the northwest, and during the DESC orbit, detection is performed from the land to the sea, whereas during the ASC orbit, detection is performed from the sea, with a tangential view of the beach and dunes. Although both ASC and DESC data align with the TWL (see Figure 14), the seasonal pattern is more pronounced in the time series from DESC, as SAR-SLs are positioned further inland due to the layover effect caused by the dunes' geometry. During periods of high TWL, SAR-SLs from DESC appear to experience a more significant retreat. In contrast, SAR-SLs from ASC are limited to the dune toe (around 150 m from the reference line). With regards to the SAR-SLs detected seawards, there are no significant differences between DESC and ASC shorelines, and the layover effect is negligible. It is remarkable that both ASC and DESC SLs in Salinas are located on ground higher than the high-water mark. More studies are necessary to identify the actual footprints that characterize the shoreline in SAR images in Salinas.

Issues related to the scene geometry were also observed in previous studies based on SAR-SLs [47,51]. Some of those studies recommend using only the SAR scenes with a shoreward view (from the sea to the continent) to avoid the scenes in which inland features obstacle the SAR signal and affect shoreline detection. However, this would reduce significantly the number of SAR-SLs detected. More studies on the interpretation the SAR signal and its relation to ground geometry are necessary.

It is worth noting that although the alignment process based on the optical image in the georeferencing phase (collocation—see Section 2.3) intends to reduce the differences

between SAR-SLs derived from ASC and DESC tracks due to these scene geometry issues (e.g., shadow/layover—see Figure A7), it does not entirely eradicate them.

4.4. Interpretation of SAR-SLs

Figure 20 summarizes our conceptual model, which partially explains the differences and similarities between the ASC and DESC SAR-SLs at the study sites. For a beach–dune–cliff system oriented west to east and different total water levels, we expect DESC SAR-SL to delineate the wet–dry beach boundary, the cliff/dune top, or the cliff/dune backshore. For the same beach–dune–cliff system, ASC SAR-SLs are more likely to delineate the wet–dry beach boundary or the cliff/dune toe, with the main reason being the presence or absence of a shadow area between the water and cliff/dune for the DESC and ASC orbits, respectively. In this figure, we have assumed a constant radar look direction and changed the water level to illustrate the different interpretations of the shoreline mapped. The radar look direction is not constant but also changes with the distance between the satellite and the feature on the ground. This simple conceptual model illustrates the importance of performing SAR visibility analysis (e.g., identifying the areas that can be affected by shadowing) for a better informed interpretation of the features being mapped.

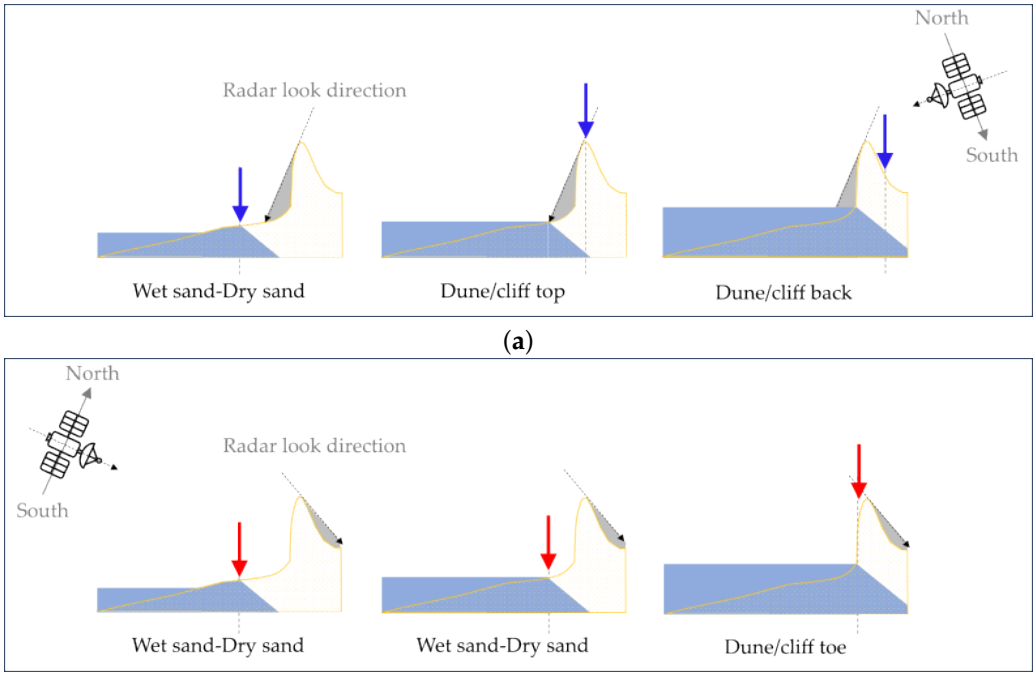

Figure 20. Interpretation of the differences between DESC (**a**) and ASC (**b**) SAR-SLs for a beach–cliff/dune system oriented west to east. Total water levels indicated in light blue, and beach surface, in yellow. Blue and red vertical arrows represent the location at which the proposed algorithm will delineate the SAR-SL.

4.5. Limitations of This Study

There are several limitations of this study that need to be considered when interpreting the results presented. Perhaps the most obvious limitation is that the three study cases chosen for this study only represent one small subset of all the different coastal environments that can be found around the world. All study cases belong to temperate places which are not regularly covered by snow or ice and do not represent the biodiversity and seasonality observed in more tropical areas. Furthermore, the coasts assessed here did not include urban beaches in which SAR-SL detection is often affected by the noise induced by man-made structures [52]. Regarding the evaluation procedures, the analysis performed on each study site is different by design, as the auxiliary data and interest in the sites differ,

providing different perspectives and complementary interpretations. The data are limited to the period between 2015 and 2021; therefore, we are unable to assess the capability of SAR-SLs to detect trends longer than 6 years for the study sites. We did not have frequent enough observations to compare the seasonal variability with ground-truth observations.

5. Conclusions

In this study, we highlighted the potential of SAR S1 data in three different sites to identify and monitor coastal morphological changes across different temporal scales. These processes encompass long-term changes in the VL, seasonal fluctuations in beach profiles, inter-annual beach rotation, and changes induced by extreme TWL events.

Overall, our analysis indicates that SAR-SL measurements consistently correspond to positions above the high-water mark across all three sites. Moreover, we demonstrated that in certain coastal settings, such as a low-lying beach (e.g., Bull Island), SAR-SLs can effectively monitor coastal change. The annual CR derived by SAR shows a very solid correlation (and low overall error) with a robust and long-term used method (SL change measured by employing time-series VLs). It has also been noted that several factors impact SAR-SL detection, including coastline orientation, coastal topography, radar signal incidence angle, backshore type, and soil moisture. Ongoing research endeavors are focusing on comprehensively understanding the influence of these factors on SAR-based SL detection and the use of the presented conceptual model, which could serve as a valuable reference for future studies focused on understanding and interpreting SAR-SLs. This deeper understanding will be instrumental in deriving consistent and accurate SAR-SLs for useful coastal change assessments.

Moreover, this research shows that SAR data offer advantages over optical data in areas where the use of optical data is challenging, as SAR S1 enables the monitoring of high-frequency coastal dynamics due to its provision of dense shoreline time-series data compared with optical S2.

In conclusion, this study illustrates the effective utilization of SAR images to monitor and understand coastal morphological changes across varying temporal scales and coastal environments. It presents a new methodology to specifically monitor some coastal settings as an alternative to what is currently available in the scientific community, and it proposes the next steps for the future research to unravel the intricate dynamics and factors influencing SAR-SL detection.

Author Contributions: Conceptualization, S.S., J.M.S., A.P., A.G.-M. and X.M.; methodology, S.S., P.G.d.S., J.M.S., A.G.T., A.P., A.G.-M. and X.M.; waterlines extraction software, S.S., M.E.P. and A.G.-M.; validation, P.G.d.S., J.M.S., A.G.T., A.P., X.M. and Y.C.; formal analysis, S.S., J.M.S., A.P., A.G.-M., X.M. and Y.C.; investigation, S.S., P.G.d.S., A.P. and X.M.; resources, A.G.T. and A.P.; data curation, S.S.; writing—original draft preparation, S.S., J.M.S., A.P. and X.M.; writing—review and editing, S.S., P.G.d.S., A.P. and X.M.; visualization, S.S., A.G.T. and A.P.; supervision, A.G.-M.; funding acquisition, J.M.S., A.P., A.G.-M. and X.M. All authors have read and agreed to the published version of the manuscript.

Funding: This work was financially supported by the Coastal Erosion From Space project, which was funded via the Science for Society allocation of the 5th Earth Observation Envelope Programme (EOEP-5) of the European Space Agency. A.P. was funded by the CHAMFER project (NE/W004992/1). This study forms part of the ThinkInAzul programme and was supported by Ministerio de Ciencia e Innovación with funding from European Union NextGeneration EU (PRTR-C17.I1) and by Comunidad de Cantabria.

Data Availability Statement: The data presented in this study are available upon request from the corresponding author.

Acknowledgments: A.P. acknowledges the contribution of Kay Smith to the initial analysis of SAR data in Start Bay. J.M.S., P.G.d.S. and A.G.T. acknowledge the Ministry for the Ecological Transition and the Demographic Challenge of the Government of Spain for providing the beach subaerial topography data used for the evaluation of the Salinas study site.

Conflicts of Interest: Authors Salvatore Savastano, Mark E. Pattle and Albert Garcia-Mondéjar were employed by the company isardSAT UK. The remaining authors declare that the research was conducted in the absence of any commercial or financial relationships that could be construed as a potential conflict of interest.

Abbreviations

The following abbreviations are used in this manuscript:

ASC	Ascending
CR	Change rate
DESC	Descending
DoD	Digital elevation model of difference
DSAS	Digital Shoreline Analysis System
DTM	Digital terrain model
SAR	Synthetic aperture radar
ESA	European Space Agency
GMD	Gaussian mixture distribution
GRD	Ground Range Detected
RL	Reference line
SL	Shoreline
S1	Sentinel-1
S2	Sentinel-2
TWL	Total water level
VL	Vegetation line

Appendix A

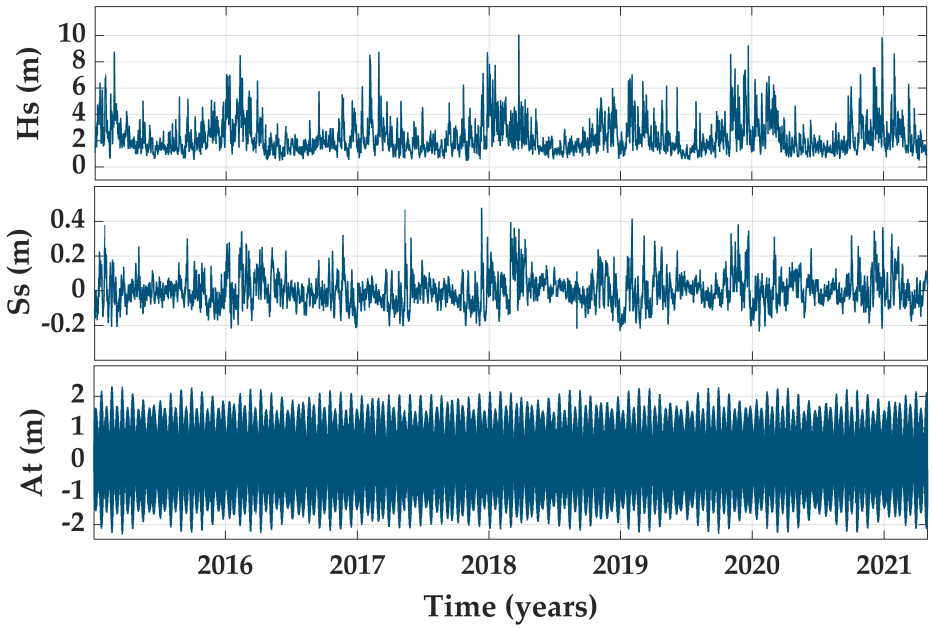

Figure A1. Wave, tide, and surge time series in Salinas beach.

Figure A2. Digital terrain models used for validation for Start Bay. For each of the time-stamped DTMs, the elevation is shown hillshaded and color-coded. Source of DTM: ©Teignbridge District Council copyright courtesy of the Southwest Regional Coastal Monitoring Programme (URL). Source of aerial imagery: Esri, Maxar, GeoEye, Earthstar Geographics, CNES/Airbus DS, USDA, USGS, AeroGRID, IGN, and the GIS User Community (v10.6). BGS ©UKRI.

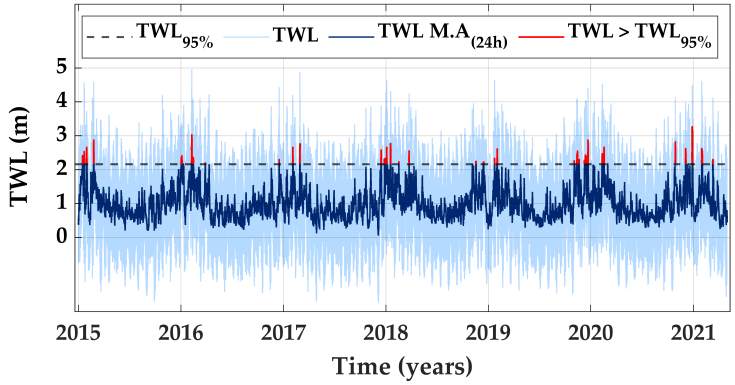

Figure A3. Total water level (TWL) time series and moving average (M.A.) based on a 24 h sampling window.

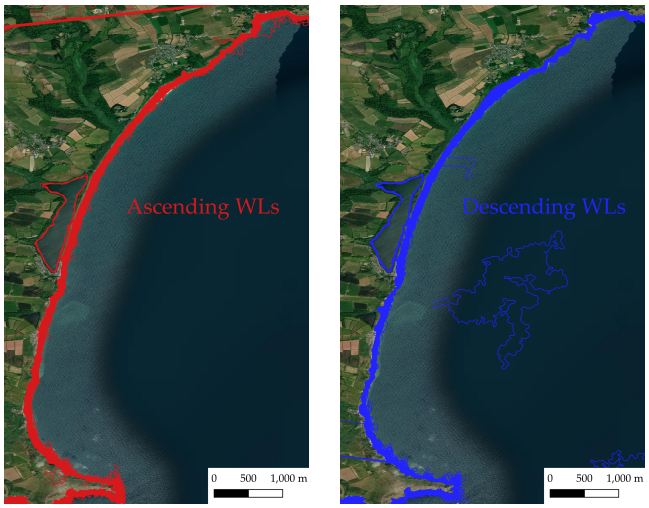

Figure A4. Location of all SLs derived from ASC (**a**) and DESC (**b**) orbits at Start Bay study site against aerial imagery. Source of aerial imagery: Esri, Maxar, GeoEye, Earthstar Geographics, CNES/Airbus DS, USDA, USGS, AeroGRID, IGN, and the GIS User Community (v10.6). BGS ©UKRI.

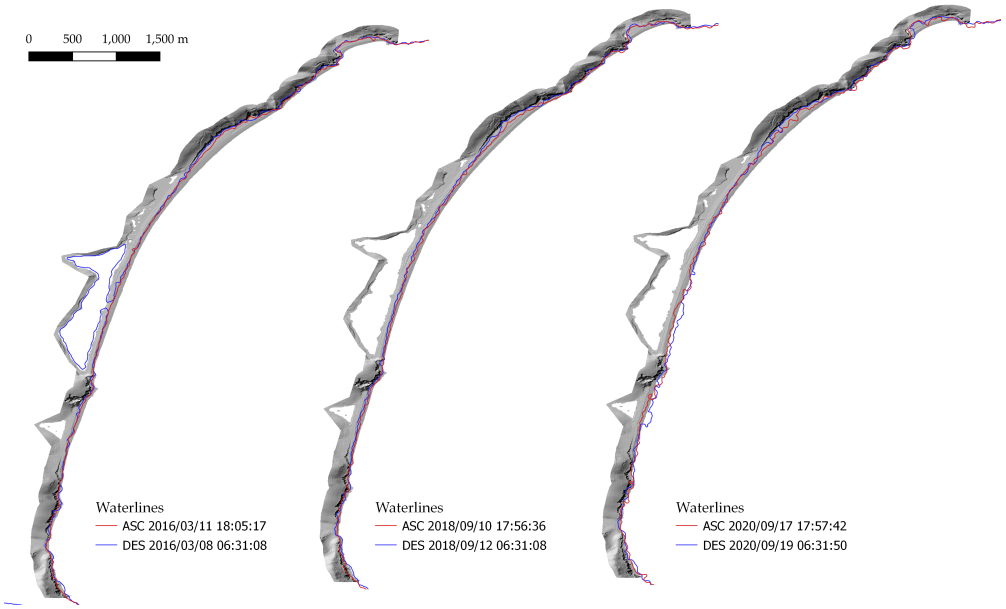

Figure A5. Location of the ASC and DESC shorelines relative to the ground-truth DTMs used in this analysis. DTMs are shown hillshaded for the years 2016, 2018, and 2020. Source of DTM: © Teignbridge District Council copyright courtesy of the Southwest Regional Coastal Monitoring Programme (URL). BGS ©UKRI.

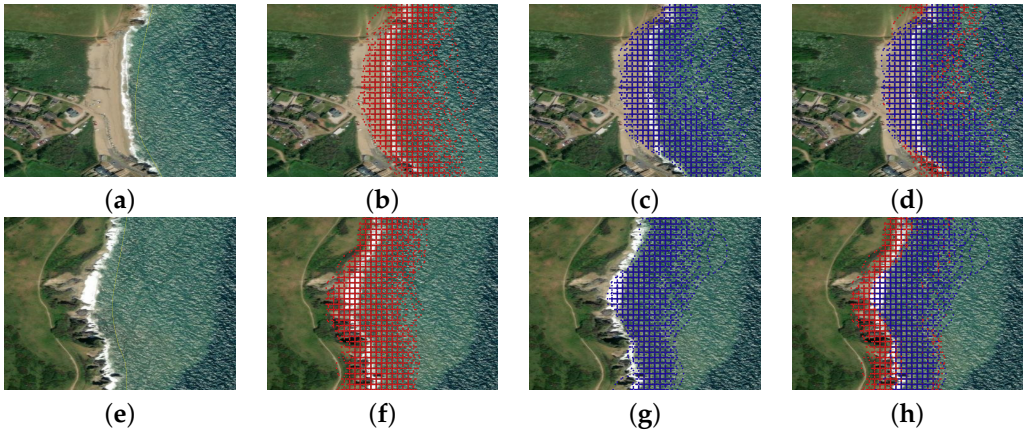

Figure A6. SLs in ASC and DESC tracks in two possible scenarios (flat beach (**a**) and cliffs (**e**)). (**b**,**f**) SLs points from ASC tracks. (**c**,**g**) SLs points from DESC tracks. (**d**,**h**) Overlapping of SLs points from ASC and DESC tracks.

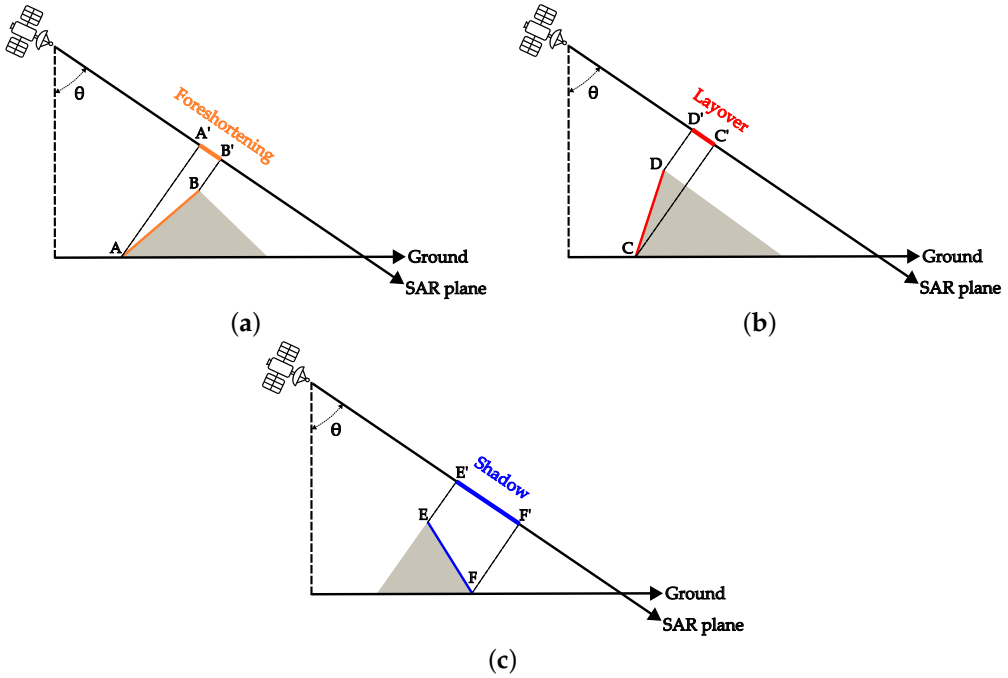

Figure A7. Geometric distortions inherent in SAR data due to the side-looking nature of the sensor, particularly in non-flat terrain. SAR detects ground points A, B, C, D, E, F as A′, B′, C′, D′, E′, F′ in the image plane, depending on the incidence angle between the satellite's line of sight and terrain elevation. (**a**) **Foreshortening**: Slope facing the sensor is compressed in the SAR image, appearing as narrow and bright bands. (**b**) **Layover**: Mountain tops can overlay the ground ahead of the mountain in the image. (**c**) **Shadow**: Slope not facing the sensor results in dark areas in the SAR image, as the sensor cannot capture these back slopes.

References

1. Mingle, J. *The Ocean and Cryosphere in a Changing Climate: Special Report of the Intergovernmental Panel on Climate Change (IPCC)*; Cambridge University Press: Cambridge, UK, 2022. [CrossRef]
2. Anfuso, G.; Bowman, D.; Danese, C.; Pranzini, E. Transect based analysis versus area based analysis to quantify shoreline displacement: Spatial resolution issues. *Environ. Monit. Assess.* **2016**, *188*, 568. [CrossRef] [PubMed]
3. Boak, E.H.; Turner, I.L. Shoreline Definition and Detection: A Review. *J. Coast. Res.* **2005**, *2005*, 688–703. [CrossRef]
4. Toure, S.; Diop, O.; Kpalma, K.; Maiga, A.S. Shoreline Detection using Optical Remote Sensing: A Review. *ISPRS Int. J.-Geo-Inf.* **2019**, *8*, 12876. [CrossRef]
5. Luijendijk, A.; Hagenaars, G.; Ranasinghe, R.; Baart, F.; Donchyts, G.; Aarninkhof, S. The state of the world's beaches. *Sci. Rep.* **2018**, *8*, 6641. [CrossRef] [PubMed]
6. Mentaschi, L.; Vousdoukas, M.I.; Pekel, J.F.; Voukouvalas, E.; Feyen, L. Global long-term observations of coastal erosion and accretion. *Sci. Rep.* **2018**, *8*, 12876. [CrossRef] [PubMed]
7. Muttitanon, W.; Tripathi, N.K. Land use/land cover changes in the coastal zone of Ban Don Bay, Thailand using Landsat 5 TM data. *Int. J. Remote Sens.* **2005**, *26*, 2311–2323. [CrossRef]
8. Hagenaars, G.; Luijendijk, A.; de Vries, S.; de Boer, W. Long term coastline monitoring derived from satellite imagery. In Proceedings of the 8th International Conference on Coastal Dynamics, Helsingør, Denmark, 12–16 June 2017; pp. 1551–1562.
9. Maglione, P.; Parente, C.; Vallario, A. Coastline extraction using high resolution WorldView-2 satellite imagery. *Eur. J. Remote Sens.* **2014**, *47*, 685–699. [CrossRef]
10. Ghosh, M.K.; Kumar, L.; Roy, C. Monitoring the coastline change of Hatiya Island in Bangladesh using remote sensing techniques. *ISPRS J. Photogramm. Remote Sens.* **2015**, *101*, 137–144. [CrossRef]
11. Curlander, J.C.; McDonough, R.N. *Synthetic Aperture Radar*; Wiley: New York, NY, USA, 1991; Volume 11.
12. Moreira, A.; Prats-Iraola, P.; Younis, M.; Krieger, G.; Hajnsek, I.; Papathanassiou, K.P. A tutorial on synthetic aperture radar. *IEEE Geosci. Remote Sens. Mag.* **2013**, *1*, 6–43. [CrossRef]
13. Ulaby, F.T.; Long, D.G.; Blackwell, W.J.; Elachi, C.; Fung, A.K.; Ruf, C.; Sarabandi, K.; Zebker, H.A.; Van Zyl, J. *Microwave Radar and Radiometric Remote Sensing*; University of Michigan Press: Ann Arbor, MI, USA, 2014; Volume 4.
14. Vos, K.; Harley, M.D.; Splinter, K.D.; Simmons, J.A.; Turner, I.L. Sub-annual to multi-decadal shoreline variability from publicly available satellite imagery. *Coast. Eng.* **2019**, *150*, 160–174. [CrossRef]

15. Paz-Delgado, M.V.; Payo, A.; Gómez-Pazo, A.; Beck, A.L.; Savastano, S. Shoreline Change from Optical and Sar Satellite Imagery at Macro-Tidal Estuarine, Cliffed Open-Coast and Gravel Pocket-Beach Environments. *J. Mar. Sci. Eng.* **2022**, *10*, 561. [CrossRef]
16. Dike, E.C.; Oyetunji, A.K.; Amaechi, C.V. Shoreline Delineation from Synthetic Aperture Radar (SAR) Imagery for High and Low Tidal States in Data-Deficient Niger Delta Region. *J. Mar. Sci. Eng.* **2023**, *11*, 1528. [CrossRef]
17. Gallagher, S.; Tiron, R.; Dias, F. A long-term nearshore wave hindcast for Ireland: Atlantic and Irish Sea coasts (1979–2012) Present wave climate and energy resource assessment. *Ocean. Dyn.* **2014**, *64*, 1163–1180. [CrossRef]
18. Wright, L.; Short, A. Morphodynamic variability of surf zones and beaches: A synthesis. *Mar. Geol.* **1984**, *56*, 93–118. [CrossRef]
19. Wiggins, M.; Scott, T.; Masselink, G.; Russell, P.; McCarroll, R.J. Coastal embayment rotation: Response to extreme events and climate control, using full embayment surveys. *Geomorphology* **2019**, *327*, 385–403. [CrossRef]
20. McCarroll, R.; Valiente, N.; Wiggins, M.; Scott, T.; Masselink, G. Coastal survey data for Perranporth Beach and Start Bay in southwest England (2006–2021). *Sci. Data* **2023**, *10*, 258. [CrossRef]
21. Chadwick, A.J.; Karunarathna, H.; Gehrels, W.R.; Massey, A.C.; O'Brien, D.; Dales, D. A new analysis of the Slapton barrier beach system, UK. *Marit. Eng.* **2005**, *158*, 147–161. [CrossRef]
22. Ruiz de Alegria-Arzaburu, A.; Masselink, G. Storm response and beach rotation on a gravel beach, Slapton Sands, U.K. *Mar. Geol.* **2010**, *278*, 77–99. [CrossRef]
23. Aulard-Macler, M. *Sentinel-1 Product Definition*; *Document Reference MPC-0240*; MacDonald, Dettwiler and Associates: Westminster, CO, USA, 2011.
24. Zollini, S.; Alicandro, M.; Cuevas-González, M.; Baiocchi, V.; Dominici, D.; Buscema, P.M. Shoreline Extraction Based on an Active Connection Matrix (ACM) Image Enhancement Strategy. *J. Mar. Sci. Eng.* **2020**, *8*, 9. [CrossRef]
25. Veci, L.; Lu, J.; Foumelis, M.; Engdahl, M. ESA's Multi-mission Sentinel-1 Toolbox. In Proceedings of the EGU General Assembly Conference Abstracts, Vienna, Austria, 23–28 April 2017; p. 19398.
26. Lee, J.S.; Wen, J.H.; Ainsworth, T.; Chen, K.S.; Chen, A. Improved Sigma Filter for Speckle Filtering of SAR Imagery. *IEEE Trans. Geosci. Remote Sens.* **2009**, *47*, 202–213. [CrossRef]
27. Marghany, M.; Sabu, Z.; Hashim, M. Mapping coastal geomorphology changes using synthetic aperture radar data. *Int. J. Phys. Sci* **2010**, *5*, 1890–1896.
28. Pradhan, B.; Rizeei, H.M.; Abdulle, A. Quantitative Assessment for Detection and Monitoring of Coastline Dynamics with Temporal RADARSAT Images. *Remote Sens.* **2018**, *10*, 1705. [CrossRef]
29. Achim, A.; Tsakalides, P.; Bezerianos, A. SAR image denoising via Bayesian wavelet shrinkage based on heavy-tailed modeling. *IEEE Trans. Geosci. Remote Sens.* **2003**, *41*, 1773–1784. [CrossRef]
30. Yu, Y.; Acton, S. Speckle reducing anisotropic diffusion. *IEEE Trans. Image Process.* **2002**, *11*, 1260–1270. [CrossRef] [PubMed]
31. Kittler, J.; Illingworth, J. Minimum error thresholding. *Pattern Recognit.* **1986**, *19*, 41–47. [CrossRef]
32. Serra, J. Image Analysis and Mathematical Morphology. *Cytometry* **1983**, *4*, 184–185.
33. Maple, C. Geometric design and space planning using the marching squares and marching cube algorithms. In Proceedings of the 2003 International Conference on Geometric Modeling and Graphics, London, UK, 16-18 July 2003; pp. 90–95. [CrossRef]
34. Schwarz, G. Estimating the Dimension of a Model. *Ann. Stat.* **1978**, *6*, 461–464. [CrossRef]
35. Leatherman, S.P. Shoreline Change Mapping and Management Along the U.S. East Coast. *J. Coast. Res.* **2003**, 5–13.
36. Himmelstoss, E.; Henderson, R.E.; Kratzmann, M.G.; Farris, A.S. *Digital Shoreline Analysis System (DSAS)*, Version 5.1 User Guide; Technical Report; U.S. Geological Survey: Reston, VA, USA, 2021. [CrossRef]
37. Genz, A.S.; Frazer, L.N.; Fletcher, C.H., Improving Statistical Validity in Calculating Erosion Hazards from Historical Shorelines. In *Coastal Sediments' 07*; American Society of Civil Engineers: Reston, VA, USA, 2007; pp. 1799–1812. [CrossRef]
38. Hapke, C.J.; Himmelstoss, E.A.; Kratzmann, M.G.; List, J.H.; Thieler, E.R. *National Assessment of Shoreline Change; Historical Shoreline Change along the New England and Mid-Atlantic Coasts*; U.S. Geological Survey: Reston, VA, USA, 2011.
39. Perez, J.; Menendez, M.; Losada, I.J. GOW2: A global wave hindcast for coastal applications. *Coast. Eng.* **2017**, *124*, 1–11. [CrossRef]
40. Egbert, G.D.; Erofeeva, S.Y. Efficient Inverse Modeling of Barotropic Ocean Tides. *J. Atmos. Ocean. Technol.* **2002**, *19*, 183–204. [CrossRef]
41. Cid, A.; Castanedo, S.; Abascal, A.J.; Menéndez, M.; Medina, R. A high resolution hindcast of the meteorological sea level component for Southern Europe: The GOS dataset. *Clim. Dyn.* **2014**, *43*, 2167–2184. [CrossRef]
42. Vos, K.; Splinter, K.D.; Harley, M.D.; Simmons, J.A.; Turner, I.L. CoastSat: A Google Earth Engine-enabled Python toolkit to extract shorelines from publicly available satellite imagery. *Environ. Model. Softw.* **2019**, *122*, 104528. [CrossRef]
43. Bell, C. *POLTIPS. 3. Applications Team at the National Oceanographic Centre*; National Oceanography Centre: Liverpool, UK, 2016.
44. Turner, J.F.; Iliffe, J.C.; Ziebart, M.K.; Wilson, C.; Horsburgh, K.J. Interpolation of Tidal Levels in the Coastal Zone for the Creation of a Hydrographic Datum. *J. Atmos. Ocean. Technol.* **2010**, *27*, 605–613. [CrossRef]
45. García, P.; Martin-Puig, C.; Roca, M. SARin mode, and a window delay approach, for coastal altimetry. *Adv. Space Res.* **2018**, *62*, 1358–1370. [CrossRef]
46. Stockdon, H.F.; Holman, R.A.; Howd, P.A.; Sallenger, A.H. Empirical parameterization of setup, swash, and runup. *Coast. Eng.* **2006**, *53*, 573–588. [CrossRef]
47. Sun, W.; Chen, C.; Yang, W.L.G.; Meng, X.; Wang, L.; Ren, K. Coastline extraction using remote sensing: A review. *Gisci. Remote Sens.* **2023**, *60*, 2243671. [CrossRef]

48. Vrijling, J.; Meijer, G. Probabilistic coastline position computations. *Coast. Eng.* **1992**, *17*, 1–23. [CrossRef]
49. Sletten, M.A.; Hwang, P.A. The Effect of Wind-Wave Growth on SAR-Based Waterline Maps. *IEEE Trans. Geosci. Remote Sens.* **2011**, *49*, 5140–5149. [CrossRef]
50. Tajima, Y.; Wu, L.; Fuse, T.; Shimozono, T.; Sato, S. Study on shoreline monitoring system based on satellite SAR imagery. *Coast. Eng. J.* **2019**, *61*, 401–421. [CrossRef]
51. Wu, L.; Tajima, Y.; Yamanaka, Y.; Shimozono, T.; Sato, S. Study on characteristics of SAR imagery around the coast for shoreline detection. *Coast. Eng. J.* **2019**, *61*, 152–170. [CrossRef]
52. Zollini, S.; Dominici, D.; Alicandro, M.; Cuevas-González, M.; Angelats, E.; Ribas, F.; Simarro, G. New Methodology for Shoreline Extraction Using Optical and Radar (SAR) Satellite Imagery. *J. Mar. Sci. Eng.* **2023**, *11*, 627. [CrossRef]